Neural Ordinary Differential Equations for Hyperspectral Image Classification

Mercedes E. Paoletti, *Student Member, IEEE,* Juan M. Haut, *Member, IEEE,* Javier Plaza, *Senior Member, IEEE,* and Antonio Plaza, *Fellow, IEEE*

***Abstract*—Advances in deep learning have allowed for the development of more complex and powerful neural architectures. The adoption of deep convolutional-based architectures with residual learning (ResNets) has reached state-of-the-art performance in hyperspectral image (HSI) classification. Traditionally, ResNets have been considered as stacks of discrete layers, where each one obtains a hidden state of the input data. This formulation must deal with very deep networks, which suffer from an important data degradation as they become deeper. Moreover, these complex models exhibit significant requirements in terms of memory, due to the amount of parameters that need to be fine-tuned. This leads to inadequate generalization and loss of accuracy. In order to address these issues, this paper redesigns the ResNet as a continuous-time evolving model, where hidden representations (or states) are obtained with respect to time (understood as the depth of the network) through the evaluation of an ordinary differential equation (ODE), which is combined with a deep neural architecture. Our experimental results, conducted with four well-known HSI datasets, indicate that redefining deep networks as continuous systems through ODEs offers flexibility when processing and classifying this kind of remotely sensed data, achieving significant performance even when very few training samples are available.**

***Index Terms*—Hyperspectral images (HSIs), deep learning (DL), ordinary differential equations (ODEs), residual networks (ResNets).**

I. Introduction

REMOTE sensing techniques have been widely employed for detecting, measuring and monitoring the physical behaviour and/or characteristics of large areas of the Earth through the acquisition and measurement of radiation emitted or reflected by the terrestrial materials that compose the observed surfaces, and which is captured by specific sensors located on airborne or spaceborne platforms [1]. The interpretation of the obtained measurements can be beneficial to human activity [2], [3]. There is a wide range of remote sensing data, where each one exhibits different spatial and spectral properties depending on the type of employed sensor and measured radiation. Moreover, current Earth observation missions are already collecting an extremely large volume of remotely sensed data from satellites and airborne systems [4]. Hyperspectral images (HSIs) are collected by passive spectrometers that measure the reflected solar radiation from the observed areas, creating huge data cubes composed by hundreds of narrow and continuous spectral wavelengths. As a result, a HSI given by $\mathbf{X} \in \mathbb{R}^{n_1 \times n_2 \times n_{bands}}$ is composed by two spatial components that determines the image's width and height ($n_1 \times n_2$) and one spectral component that indicates the number of channels or spectral bands (n_{bands}). As a result, each pixel of $\mathbf{X}$ can be interpreted as a detailed spectral signature or spectral vector $\mathbf{x}_i \in \mathbb{R}^{n_{bands}} = \{x_{i,1}, \cdots, x_{i,n_{bands}}\}$, which allows for an accurate characterization of the surface materials [5]. This has attracted the attention of many researchers that employ HSIs into a wide range of applications, including precision agriculture [6], environment and natural resources management [7], mineralogy [8], forestry [9], disaster monitoring [10], urban planning [11], and defense applications [12], among others.

A large variety of algorithms have been developed to process and extract useful information from HSI data cubes. In this regard, HSI classification methods can greatly benefit from the rich spectral information contained in each pixel $\mathbf{x}_i$. In fact, the classification of these images aims to assign a single category (or label) to each pixel in the image. In mathematical fashion, the goal of a classifier is to approximate a mapping function of the form $f(\cdot, \theta)$, which depends on parameters θ, to map the pixels in the original HSI $\mathcal{X} \subset \mathbb{R}^{n_{samples}}$ to those labels contained in a set of categories $\mathcal{Y} \subset \mathbb{N}$, i.e., $f : \mathcal{X} \rightarrow \mathcal{Y}$. In the particular case of HSI classification, the procedure consists of mapping each pixel $\mathbf{x}_i$ in $\mathbf{X} \equiv \{\mathbf{x}_1, \cdots, \mathbf{x}_{n_{samples}}\}$ (with $n_{samples} = n_1 \cdot n_2$) to an unique numerical label of $n_{classes}$ possible classes $y_i = \{1, \cdots, n_{classes}\}$, extracted from the set $Y \equiv \{y_1, \cdots, y_{n_{samples}}\}$, creating pairs of $\{\mathbf{x}_i, y_i\}_{i=1}^{n_{samples}}$ for each spectral pixel.

Traditional HSI classification methods are based on the analysis of the each pixel $\mathbf{x}_i$ independently, without considering spatial information. For instance, unsupervised clustering techniques such as k-means [13] and supervised or semi-supervised methods, as the widely-used support vector machine (SVM) [14] or multinomial logistic regression (MLR)

This work has been supported by Ministerio de Educación (Resolución de 26 de diciembre de 2014 y de 19 de noviembre de 2015, de la Secretaría de Estado de Educación, Formación Profesional y Universidades, por la que se convocan ayudas para la formación de profesorado universitario, de los subprogramas de Formación y de Movilidad incluidos en el Programa Estatal de Promoción del Talento y su Empleabilidad, en el marco del Plan Estatal de Investigación Científica y Técnica y de Innovación 2013-2016. This work has been supported by Junta de Extremadura (Decreto 14/2018, de 6 de febrero, por el que se establecen las bases reguladoras de las ayudas para la realizacin de actividades de investigacin y desarrollo tecnolgico, de divulgacin y de transferencia de conocimiento por los Grupos de Investigacin de Extremadura, Ref. GR18060) and the European Union's Horizon 2020 research and innovation programme under grant agreement No. 734541 (EOXPOSURE). Funding from MINECO project TIN2015-63646-C5-5-R is gratefully acknowledged. *(Corresponding author: Mercedes E. Paoletti)*

M. E. Paoletti, J. M. Haut, J. Plaza and A. Plaza are with the Hyperspectral Computing Laboratory, Department of Technology of Computers and Communications, Escuela Politécnica, University of Extremadura, 10003 Cáceres, Spain.(e-mail: mpaoletti@unex.es; juanmariohaut@unex.es; jplaza@unex.es; aplaza@unex.es).

[15], among others [16], [17]. Artificial neural networks (ANNs) [18], [19] have acquired great popularity due to their flexibility concerning learning modes (unsupervised, supervised and semi-supervised) and available architectures (shallow, deep, fully or local connected). Moreover, ANNs work as universal approximators [20], [21], being able to extract representative features and to discover nonlinear relationships from the input data.

Advances in deep learning [22], [23] have allowed for the implementation of deeper and more complex ANNs, known as deep neural networks (DNNs). These networks are composed by groups of neurons organized into a hierarchy of multiple nonlinear layers, which are stacked one by one. As a result, DNNs are composed by one input and one output layer, with several hidden layers in-between them. The original data goes through the hierarchy of layers, where a different level of data representation is obtained at each layer. These representations are composed by highly expressive features that encode complex patterns and nonlinear relationships in the data. At the end of the network, highly abstract and discriminative information is obtained, which can be employed to enhance classification tasks. In the following, we briefly review some recent deep learning works in the literature (focusing on those based on convolutional and residual architectures for HSI data classification), and then we discuss some shortcomings and limitations of these works and the solutions adopted in this paper.

A. Recent Trends in Deep Learning for HSI Classification

DNNs traditionally follow a biological neural model, implementing a fully-connected (FC) topology where all the neurons in a layer are totally connected with all the neurons of the previous and following layers, as in the multilayer perceptron (MLP). In this way, each neuron applies a dot product between the outputs of previous neurons and the connection weights, simulating synaptic weights. The obtained result is filtered by a threshold function, also known as nonlinear activation function, which encodes the nonlinearities of the data and triggers (or not) the activation of a given neuron. In fact, DNN approaches adopt the same strategy as traditional pixel-wise classifiers. For HSI data, they take as input the spectral pixels of the HSI data cube [18]. In this regard, spectral-based DNNs are quite sensitive to variations in the spectral signatures. It should be noted that HSI data are characterized by their high intra-class variability and inter-class similarity (due to perturbations and disturbances in the data collection process at the spectrometer, atmospheric conditions, etc.) Also, HSI data normally exhibit low spatial resolution, which means that a single pixel often contains multiple materials, resulting in mixed spectral signatures. These shortcomings, coupled with the curse of dimensionality and the Hughes phenomenon [24] (which establishes the need for a reasonable balance between the number of training samples and the number of spectral bands in order to ensure a reliable classification [25], [26]) are important challenges to deploy the full potential of HSI technology with traditional pixel-based DNN approaches.

A significant evolution in deep learning techniques was the adaptation of biological visual cortex neurons into DNN architectures, with the implementation of convolutional neural networks (CNNs) [22]. Inspired by the local receptive field of such visual cortex neurons (activated or not in the presence of certain types of visual stimuli), CNN-based models rely on the application of a sliding n-dimensional kernel on the input data of each layer. This allows for the exploitation of the visual properties of an image, learning features at certain positions of such image, and applying these features as filters to the rest of the image in order to obtain a feature-activation map [27], [28]. In this sense, the contextualization provided by the spatial components $n_1 \times n_2$ of the HSI data cube $\mathbf{X}$ can greatly reduce the variability of spectral samples by interpreting the data surrounding the pixels as belonging to the same class, which reinforces the information contained in the target pixel, reducing also the well-known "salt & pepper" noise of spectral classifiers.

CNN models exhibit excellent performance in HSI data classification through the development of a wide range of architectures, from traditional spectral-based ones (CNN1D) to spatial (CNN2D) and spectral-spatial (CNN3D) models. For instance Hu *et al.* [29] implemented a five-layer CNN1D to classify HSI data in the spectral domain, and Yue *et al.* [30] developed a CNN3D to classify HSI data taking into account spectral-spatial information. Zhao *et al.* [31] exploited a CNN2D model as a highly confident spatial feature extractor. Chen *et al.* [32] reviewed CNN1D, CNN2D and CNN3D models for deep HSI feature extraction and classification. In order to enhance the classification results, several improvements have been added to the CNN architecture. For instance, Yu *et al.* [33] implemented a three-layer CNN2D model with 1×1 kernels, inspired by the network in network (NIN) model [34] in order to overcome the presence of highly correlated bands in the HSI data cube. He *et al* [35] combined the information contained in HSI-extracted covariances with a CNN2D model. The authors in [36] presented a faster end-to-end CNN3D that improved the classification accuracy taking into account the full spectral signatures contained in HSI data.

Despite the aforementioned results, CNN models still face certain limitations related to the intrinsic characteristics of HSI data and the (high) number of parameters and the depth of the network. In particular, CNNs need a large amount of training data to properly adjust their weights [37]. They also require some variability in the data in order to extract more features [28]. Although HSI data often exhibits a wide variety of samples, very limited labeled data are often available due to their high cost, which in the end hampers the feature extraction process and leads to over-adjustment (overfitting) in the convolutional model's parameters.

In addition, the implementation of very deep CNN models through the stacking of successive layers has proved to be inefficient itself [38], since a significant degradation can be observed in both the forward propagation of the data and the back-propagation of the gradient signal through the layers (vanishing gradient problem) [39], [40]. To overcome these issues, the residual learning aims to facilitate data re-usability through identity functions implemented by skip or residual connections. Residual networks (ResNets) [38] and other residual-based architectures (such as highway networks [41],

DenseNets [42] or ResNets of Resnets -RoRs- [43]) have emerged as the current state-of-the-art in image processing [44], allowing for the development of highly complex and deep architectures, using hundreds to thousands of layers [45]. These techniques, aimed at enhancing the propagation of data through the network, have been successfully adopted in several HSI classification works [46], [47], [48].

However, ResNets exhibit some shortcomings in terms of architecture optimization. In fact, residual-based models for HSI classification are quite sensitive to minor architectural changes, in particular, the selection of an appropriate kernel size has a significant impact on the final classification accuracy, due to the low spatial resolution of HSI data cubes [47]. In contrast, at certain levels of depth, adding more or less layers to the network does not impact the classification result significantly [48]. In turn, this obviously affects the number of parameters that must be stored and trained. The understanding of the optimal number of parameters required by a certain architecture (number of layers, kernel sizes, etc.) is quite critical, but it is often hand-crafted and adjusted by trial and error.

B. Re-thinking the ResNet model for HSI classification

DNNs (in general) and ResNets (in particular) have been interpreted as a discrete sequence of L stacked layers, where each one applies its transformation to the input data until reaching a final classification decision, which is performed by the last layer. This implies that the ResNet model is evaluated at fixed intervals of "time", defined by the layer depth. Also, assuming that each layer has the same number of neurons $n_{neurons}$ (which can be interpreted as the kernel's size in the convolutional architecture), the number of trainable parameters depends directly on L, so the complexity of the network (and its memory consumption) grows linearly with $\mathcal{O}(L)$ order, which could have an impact on the model's overfitting. Under the same assumption, the computation time of the inference stage also depends on L.

The aforementioned implications provide an idea of the importance of the model's depth. As a result, the selection of L must be carefully done. In fact, the main goal of the present work is focused on two important aspects: i) checking the effects of the depth when $L \to \infty$, and ii) analyzing strategies to provide the network with constant and low memory cost (in terms of the number of parameters). In this context, the feature extraction (FE) function applied by each residual unit can be interpreted as the explicit Euler discretization of a continuous-time transformation [49], [50]. Following this interpretation, the entire ResNet model can be described through an ordinary differential equation (ODE) [51], [52], whose evaluation at different times will determine the model's solution [53], [54].

With the aforementioned ideas in mind, the main contribution of this work is to redefine the traditional architecture of the ResNet model (in the context of HSI data classification) by means of a continuous-time vision using ODEs, developing a residual-based DNN with a significantly reduced number of trainable parameters (thus effectively dealing with overfitting issues) and constant and low memory cost. These are important advantages in the area of HSI classification. More specifically, this work proposes for the first time in the literature the implementation of a continuous-depth ResNet with a parameterized spectral-spatial ODE in order to perform HSI data classification.

The remainder of this paper is organized as follows. Section II introduces our newly developed model (called hereinafter ODEnet). Section III validates the newly proposed model by providing a detailed discussion of the results obtained using four widely-used HSI data sets. Finally, section IV concludes the paper with some remarks and hints at plausible future research lines.

II. Methodology

A. Residual Units as Discrete Steps of Blocks

DNN architectures are stacks of L hidden blocks [55] F_1 to F_L, where each one F_l is given by the following mapping function:

$$\mathbf{X}^{(l)} = F_l\left(\mathbf{X}^{(l-1)}, \mathbf{W}^{(l)}, b^{(l)}\right), \tag{1}$$

where $\mathbf{X}^{(l-1)}$ and $\mathbf{X}^{(l)}$ are the input and output data, respectively, and $\mathbf{W}^{(l)}$ and $b^{(l)}$ are the weights and biases of the l-th mapping function F_l. In order to address the classification problem $f : \mathcal{X} \to \mathcal{Y}$, the DNN model assigns a classification map $\mathbf{Y} \in \mathbb{R}^{n_{samples}}$ to the given input $\mathbf{X} \in \mathbb{R}^{n_{samples} \times n_{bands}}$ by applying L sequential operations defined by Eq. (1). In this sense, the classification function $f(\cdot, \theta)$ can be re-interpreted as the concatenation of the processing at each each layer processing as follows:

$$\mathbf{Y} = f(\mathbf{X}, \theta) = \hat{F}(F_L(F_{L-1}(\cdots F_1(\mathbf{X}) \cdots))), \tag{2}$$

being $\mathbf{X}$ the original input data, $F_l(\cdot)$ the mapping function performed by the l-th network's block, and $\hat{F}(\cdot)$ the final classification layer, while θ comprises the network's parameters [49]. In this regard, instead of considering the classification mapping as a global problem, the DNN model splits it into L mapping functions F_l, where the goal of the classification is to learn the parameters of each F_l that better minimize the convex loss function given by Eq. (3):

$$E = \frac{1}{n_{samples}} \sum_{i=1}^{n_{samples}} \parallel f(\mathbf{X}_i, \theta) - \mathbf{X}_i \parallel_2 . \tag{3}$$

If we focus on convolutional-based models, the data transformation defined by Eq. (1) is tailored in a FE stage defined by a *kernel operation* [36], which allows to easily combine the spatial-contextual information with the spectral information. In this context, the CNN maintains the original 3-dimensional data structure, adding a lot of flexibility to the model and a natural way to include the spectral-spatial information. Moreover, the internal structure of the CNN's layers and their operations (based on local receptive fields) have promoted it as a highly accurate feature extractor.

Two main parts can be observed in an end-to-end CNN classifier network: i) the *FE stack*, which obtains high-level representations of the input data (also feature maps) and is usually composed by a hierarchy of convolutional, nonlinear and subsampling layers, among others, and ii) the *FC classifier*,

which actually labels the data from the previously obtained feature maps and is implemented as a standard MLP.

Focusing on the FE stack, it is usually adopted to implement an architecture of several hierarchically stacked extraction and detection stages, where the l-th stage defines the l-th mapping function F_l, following the notation of Eq. (1). Moreover, each F_l is usually composed by: i) the *convolutional layer*, ii) the *nonlinear layer*, iii) the *normalization layer*, and iv) the *pooling layer*, as Eq. (4) shows, although both the order and the type of layers may vary from one CNN architecture to another (even from one stage to another).

$$\mathbf{A}^{(l)} = \left(\mathbf{W}^{(l)} *_{k\times k\times q} \mathbf{X}^{(l-1)}\right) + b^{(l)} \tag{4a}$$

$$\hat{\mathbf{A}}^{(l)} = \frac{\mathbf{A}^{(l)} - \text{mean}\left[\mathbf{A}^{(l)}\right]}{\sqrt{\text{var}\left[\mathbf{A}^{(l)}\right] + \epsilon}} \cdot \gamma + \beta \tag{4b}$$

$$\tilde{\mathbf{A}}^{(l)} = \mathcal{H}\left(\hat{\mathbf{A}}^{(l)}\right) \tag{4c}$$

$$\mathbf{X}^{(l)} = \mathcal{P}_{k\times k}\left(\tilde{\mathbf{A}}^{(l)}\right) \tag{4d}$$

The convolutional layer performs the basic FE task of the model. The spectral-spatial convolutional layer of the F_l mapping function is composed by a group of K filters, with $\mathbf{W}^{(l)} \in \mathbb{R}^{k\times k\times q}$ weights and $b^{(l)}$ biases, being $k \times k \times q$ the local receptive field of the layer. In consequence, each layer creates a linear kernel that slides (following a stride s) and overlaps the input data, convolving ($*$) its filters on local patches of the data, as Eq. (4a) indicates. As a result, the obtained output volume is composed by K feature maps.

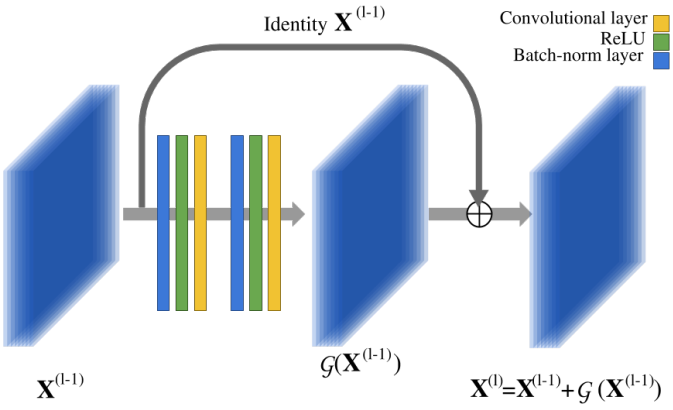

Fig. 1. Graphical representation of the l-th residual unit architecture, F^l, composed by two feature extraction and detection stages. Each stage is composed by normalization, nonlinear and convolutional layers. The application of these stages gives as a result the output volume $\mathcal{G}(\mathbf{X}^{(l-1)})$, to which an identity mapping is added at the end of the residual unit, obtaining the final residual output volume $\mathbf{X}^{(l)} = \mathbf{X}^{(l-1)} + \mathcal{G}(\mathbf{X}^{(l-1)})$.

After the convolutional layer, it is common to include a batch normalization layer, which imposes a Gaussian distribution on the obtained feature maps with the aim of preventing the data degradation and vanishing gradient problems (mainly due to the covariance shift that the data suffers). Eq. (4b) gives the regularization expression, where ϵ is a parameter that allows a certain numerical stability and γ and β are learnable parameters.

Following the normalization layer, a nonlinear layer $\mathcal{H}(\cdot)$ defined by Eq. (4c) is introduced in order to extract the activation maps from the convolutional output volume. In fact, this layer embeds a nonlinear activation function, which encodes the detector stage of the network [56], learning the nonlinear representations and relationships inside the data. Many activation functions can be selected, such as the tanh, sigmoid or rectified linear unit (ReLU) [57], which allows a faster training of the model due to its high computational efficiency.

Finally, the extraction and detection stage ends with the pooling layer $\mathcal{P}_{k\times k}(\cdot)$ given by Eq. (4d), which performs a downsampling strategy with the aim of reducing the spatial dimensions of the output volume by applying, for instance, a max, average, or sum operation on the spatial receptive field of dimensions $k \times k$.

Based on the CNN architecture, the success of the ResNet model lies in the skip and residual connections, in which grouped operation layers (i.e. convolutional, pooling and normalizing layers) and nonlinear activation functions compose the basic blocks for data mapping [47], as shown in Fig. 1. These residual units allow for the development of deeper architectures, where the inputs and outputs of each unit are connected through a residual connection, performing an additional identity mapping that allows to propagate the information from previous blocks to the rest of the network. In this context, for the l-th residual unit, the feature extraction and detection stage given by Eq. (4) can be reformulated as follows:

$$\mathbf{A}^{(l)} = \mathbf{X}^{(l-1)} + \mathcal{G}\left(\mathcal{W}^{(l)}, \mathbf{X}^{(l-1)}, \mathcal{B}^{(l)}\right) \tag{5a}$$

$$\mathbf{X}^{(l)} = \mathcal{H}(\mathbf{A}^{(l)}) \tag{5b}$$

where $\mathcal{G}(\cdot)$ comprises all the operations applied over the residual unit's input data, i.e. all the convolutions, poolings, normalizations and activations applied over $\mathbf{X}^{(l)}$, being $\mathcal{W}^{(l)}$ and $\mathcal{B}^{(l)}$ the weights and biases of the layers involved in the residual block, respectively. Moreover, the additive residual mapping function added to $\mathcal{G}(\cdot)$ allows to recycle the features obtained at the previous level of abstraction.

Following Eq. (2), the ResNet defines each mapping function F_l through Eq. (5). In this context, the neural model can be interpreted as a discrete sequence of L hidden units or mapping functions, dividing the classification process into L steps, so that each F_l defines a hidden *state* of the process, which becomes more manageable, with simple and detailed steps that allow for a more accurate final classification. However, this implies that the quality of the model depends on its trainable parameters, and the number of trainable parameters depends directly on L. This has two main implications. On the one hand, the memory consumption grows linearly [with $\mathcal{O}(L)$ order] and there is an increment of training data that the model must assume in order to properly learn the network's parameters, avoiding the overfitting problem. On the other hand, although the residual connections alleviate the aforementioned problem, each new unit that is added to the model introduces a small error [38], [58], which may hinders

the model's overall performance. These issues are particularly critical when dealing with highly variable HSI data sets.

B. Residual Units as Discrete Steps of ODEs

Our goal is to develop a residual model with constant and low memory cost, through a significant reduction of the number of trainable parameters. We follow the premise of traditional optimization models: solving a lot of small steps is often better than solving fewer and more complex ones [50]. In this sense, and following Eq. (2), we propose to implement a ResNet model for HSI data classification in which the forward problem is composed by infinitesimal steps, i.e. $L \rightarrow \infty$ [54]. Each of these steps performs Eq. (5), which describes an explicit Euler discretization step of the ODE [51], [52]. Below, the mathematical relationship between ResNet models and ODEs is described in detail.

We focus on first-order ODE expressions. Following Euler's solving method, any first-order ODE can be expressed as an initial value problem (IVP) of the form:

$$\frac{\mathrm{d}\mathbf{z}(t)}{\mathrm{d}t} = f(t, \mathbf{z}(t), \theta), \text{ with } \mathbf{z}(t_0) = \mathbf{z}_0, \tag{6}$$

where t_i is an independent variable defined in terms of *time* in an observation interval $\{0, ..., T\}$, $f(\mathbf{z}(t), t, \theta)$ is a known and continuous function with parameters θ, and $\mathbf{z}(t)$ is the unknown function that must be approximated, with initial state $\mathbf{z}_0$ at time t_0. In fact, the goal of any ODE function is to recover the closest and most accurate value $\mathbf{z}_i$ of the unknown function $\mathbf{z}(t_i)$ at each observation point t_i.

From a geometric point of view, knowing $\mathbf{z}(t_0) = \mathbf{z}_0$, an approximation of $\mathbf{z}(t_i) = \mathbf{z}_i$ in any step t_i can be performed by drawing the tangent line from previous-known points as follows:

$$\mathbf{z}_1 \approx \mathbf{z}_0 + f(t_0, \mathbf{z}_0, \theta)(t_1 - t_0) \tag{7a}$$

$$\mathbf{z}_i \approx \mathbf{z}_{i-1} + f(t_{i-1}, \mathbf{z}_{i-1}, \theta)(t_i - t_{i-1}) \tag{7b}$$

$$\mathbf{z}_T \approx \mathbf{z}_{T-1} + f(t_{T-1}, \mathbf{z}_{T-1}, \theta)(t_T - t_{T-1}) \tag{7c}$$

Generalizing the discrete steps defined above, it can be stated that any $\mathbf{z}(t_i)$ can be approximated by Eq. (7b). Assuming that the i-th observation point is connected to the first one (following the relation $t_i = t_0 + \alpha \cdot i$, where α is a step-size), the Euler discretization method claims that each point t_i is related to the immediately preceding one, t_{i-1}, through the step-size α as follows: $t_i = t_{i-1} + \alpha$. Including this relationship in Eq. (7b), the Euler's method gives a solution for $\mathbf{z}(t_i)$ as:

$$\mathbf{z}_i = \mathbf{z}_{i-1} + f(t_{i-1}, \mathbf{z}_{i-1}, \theta) \cdot (\cancel{t_{i-1}} + \alpha - \cancel{t_{i-1}}) \tag{8a}$$

$$\mathbf{z}_i = \mathbf{z}_{i-1} + \alpha \cdot f(t_{i-1}, \mathbf{z}_{i-1}, \theta) \tag{8b}$$

At this point, it is easy to observe the relationship between the ResNet model and the first-order ODE. Focusing on Eq. (5), we can simplify it into a more condensed form:

$$\mathbf{X}^{(l)} = \mathbf{X}^{(l-1)} + \mathcal{G}(\mathbf{X}^{(l-1)}, \theta_l) \tag{9}$$

The similarities between Eq. (8b) and Eq. (9) are evident. In fact, Eq. (9) defines an explicit Euler discretization step of a first-order ODE, where the step-size is set to $\alpha = 1$ and the known function is implemented by the extraction and detection stages $\mathcal{G}(\cdot)$ of the residual unit, being parameterized by the weights and biases of the layers that compose the residual unit $\theta_l = (\mathcal{W}^{(l)}, \mathcal{B}^{(l)})$. In other words, the ODE function is, in fact, a CNN.

Following this intuition, we can replace the discrete block-by-block performance of a ResNet model by a continuous-time ODE function. In particular, we assume a residual model with $L \rightarrow \infty$ equal residual units. In this sense, each mapping function F_l has to perform the same extraction and detection stages in $\mathcal{G}(\cdot)$, so each unit has the same number of parameters θ and works in the same feature space $F_1, \cdots, F_L \in \mathbb{R}^{\hat{n}_1 \times \hat{n}_2 \times \hat{n}_3}$, where $\hat{n}_1 \times \hat{n}_2 \times \hat{n}_3$ are the spatial-spectral dimensions of the feature maps.

In this way, the successive transformations given by Eq. (2), $F_1, \cdots, F_L$, can be interpreted as the continuous mapping function $F(t)$, evaluated at different times (with a relationship between layers and time). So, at the i-th observation time, we can obtain $F(t_i) = \mathbf{X}_i$. As a result, the residual model can be reformulated as the ODE in Eq. (10), which gives the discretization step of Euler's method and the expression of the first-order ODE:

$$\mathbf{X}_i = \mathbf{X}_{i-1} + \mathcal{G}(t_{i-1}, \mathbf{X}_{i-1}, \theta), \tag{10a}$$

$$\text{where } \frac{\mathrm{d}F(t)}{\mathrm{d}t} = \mathcal{G}\left(t, F(t), \theta\right), \text{ with } F(t_0) = \mathbf{X}_0. \tag{10b}$$

As it can be observed, the ODE is implemented by the neural network defined by $\mathcal{G}(\cdot)$, and parameterized by θ.

C. Proposed ODEnet for HSI Classification

We propose, for the first time in the literature, to reinterpret the ResNet model (for HSI data classification) as a continuous transformation given by the first-order ODE described in Eq. (10). Fig. 2 gives a general overview of the proposed ODEnet, which receives as input the HSI data cube with dimensions $\mathbf{X} \in \mathbb{R}^{d \times d \times n_{bands}}$. In fact, the model is fed with hyperspectral patches cropped from the original HSI cube, composed by $d \times d$ pixels and n_{bands} spectral bands, where the label corresponds to the central pixel of the patch. Also, in order to take advantage of border pixels, a mechanism for mirroring the image edges has been implemented [36].

The proposed network architecture is divided into the FE-layers and the final classification layers. Focusing on the FE-layers, they are grouped in three categories: i) FE-head, ii) FE-body, and iii) FE-tail. The FE-head performs a downsampling of the data, reducing noise and cleaning the information contained in the input. It is composed by a convolutional layer F_1 and a residual unit F_2. F_1 prepares the input data, extracting the initial features from the HSI cube, which are fundamental to the performance of the rest of the layers. During the training process, these features will become more and more robust and discriminative, being decisive for the final classification. F_2 has been implemented following the *pre-activation* architecture proposed in [45], performing data downsampling and it is composed by two FE and detection stages with normalization, nonlinear and convolutional layers, adding a convolutional layer on the skip connection to maintain the data shape.

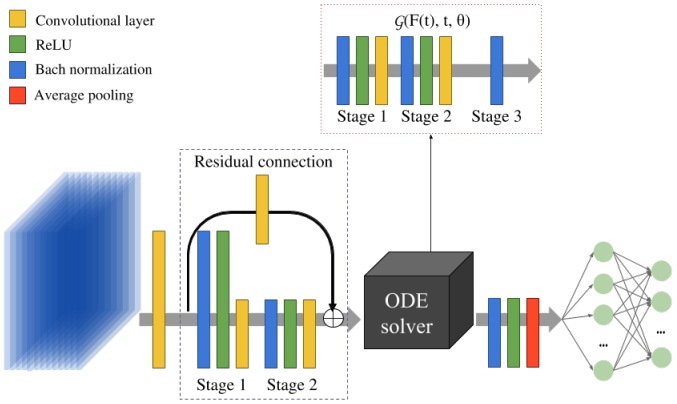

Fig. 2. Architecture of the proposed ODEnet for HSI data classification. The feature extractor part is composed by three well-differentiated parts: (i) a pre-processing step that filters the spatial-spectral noise and extracts low-level feature representations, (ii) the ODE solver, that evaluates the function $\mathcal{G}(\cdot)$ defined by a neural network and whose output, after being refined (iii), is employed to perform the final classification, implemented by two fully-connected layers.

The obtained features are sent to the FE-body, which is implemented by a continuous-time ResNet. In this context, the ODE implemented by Eq. (10) has been parameterized by a CNN model. As Fig. 2 shows, this model follows the *pre-activation* architecture [45] and has three stages, where each one is composed by normalization, nonlinear and convolutional layers (stages 1 and 2), and a normalization layer (stage 3). This ODE is solved from some initial time t_0 to some ending time t_T, creating an integration time interval $[0, T]$. Furthermore, during each forward-pass, the traditional discrete-layer execution of the model is eventually replaced by $\hat{L}$ evaluations of Eq. (10), performed by a black-box solver in the interval $[0, T]$, which receives as the initial condition $\mathbf{X}_0$ the output of F_2, the known function $\mathcal{G}(\cdot)$ and its parameters θ, in addition to the integration time interval, and a tolerance threshold of the estimated error, tol:

$$F(t_T) = \mathbf{X}_T = \mathit{ODEsolver}\left(\mathbf{X}_0, \mathcal{G}, \theta, [t_0, t_T], tol\right) \quad (11)$$

Eq. (11) can be performed by any off-the-shelf ODE solver. There is a great variety of methods for this purpose, grouped in different categories depending on their internal characteristics and working modes [59], being some of the methods framed within the Runge-Kutta family the most well-known:

- *Forward Euler*. This is the most popular numerical explicit method for solving first-order ODEs. It is also the simplest method to implement, where the new states are obtained through previously known ones by the intersection of tangent lines, as Eq. (8) shows. Given the first-order ODE of Eq. (6), and using α as the step-size, the approximation error of Euler's discretization method will be proportional to $\mathcal{O}(\alpha^2)$.
- *Explicit midpoint method*, also known as *modified Euler method*. Given Eq. (6) the evaluations are made at $\alpha/2$, so this method determines the value $\mathbf{z}(t_i) = \mathbf{z}_i$ as the following approximation:

$$\mathbf{z}_i = \mathbf{z}_{i-1} + \alpha \cdot f\left(t_{i-1} + \frac{\alpha}{2}, \mathbf{z}_{i-1} + \frac{\alpha}{2} \cdot k_1\right) \quad (13a)$$

$$k_1 = f(t_{i-1}, \mathbf{z}_{i-1}) \quad (13b)$$

This method reduces the estimation error when the Euler's step-size is too high and the tangent needs to be elongated to find the intersection point.

- *Fourth-order Runge-Kutta method (RK4)*. This is the most widely used method of the Runge-Kutta family. Inspired by the midpoint method, the basic idea is that, given two equidistant points $t_i = t_{i-1} + \alpha$, the function $\mathbf{z}(t_i) = \mathbf{z}_i$ can be approximated as the sum of the previously known value and the weighted average of s slopes [60]:

$$\mathbf{z}_i = \mathbf{z}_{i-1} + \sum_{n=1}^{s} b_n, k_n \quad (14a)$$

$$k_1 = \alpha f(t_{i-1}, \mathbf{z}_{i-1}) \quad (14b)$$

$$k_n = \alpha f\left(t_{i-1} + c_n\alpha, \mathbf{z}_{i-1} + \sum_{\hat{n}=1}^{n-1} a_{n,\hat{n}} k_{\hat{n}}\right) \quad (14c)$$

where $a_{n,\hat{n}}$, b_n and c_n are weighted coefficients. In this sense, given Eq. (6), the RK4 method determines the value at t_i as an approximation of the previously known $\mathbf{z}_{i-1}$ and the weighted average of four increments: $(k_1 + 2k_2 + 2k_3 + k_4)/6$, which are calculated on certain points of the slope defined by $f(\mathbf{z}(t), t, \theta)$, in particular, the starting, ending and midpoints [61]:

$$\mathbf{z}_i = \mathbf{z}_{i-1} \cdot \frac{1}{6}(k_1 + 2 \cdot k_2 + 2 \cdot k_3 + k_4) \quad (15a)$$

$$k_1 = \alpha f(t_{i-1}, \mathbf{z}_{i-1}) \quad (15b)$$

$$k_2 = \alpha f(t_{i-1} + \frac{\alpha}{2}, \mathbf{z}_{i-1} + \frac{k_1}{2}) \quad (15c)$$

$$k_3 = \alpha f(t_{i-1} + \frac{\alpha}{2}, \mathbf{z}_{i-1} + \frac{k_2}{2}) \quad (15d)$$

$$k_4 = \alpha f(t_{i-1} + \alpha, \mathbf{z}_{i-1} + k_3) \quad (15e)$$

Following Eq. (15), the approximation error is proportional to $\mathcal{O}(\alpha^4)$, being more precise than the two previous methods.

- *Dormand-Prince method (DOPRI5)*. This is an explicit and adaptive Runge-Kutta method to calculate fourth and fifth-order solutions. In fact, following Eq. (14), it calculates seven slopes: k_1, k_2, k_3, k_4, k_5, k_6 and k_7, which are employed to calculate two approximations of $\mathbf{z}(t_i) = \mathbf{z}_i$ by two different linear combinations. Eq. (12a) gives the first approximation, with $\mathcal{O}(\alpha^4)$ order, while Eq. (12b) gives the second approximation, with $\mathcal{O}(\alpha^5)$ order. An interesting aspect of DOPRI5 solver is its ability to adapt the step-size α to keep the estimated error $|\hat{\mathbf{z}}_i - \mathbf{z}_i|$ below a pre-defined threshold. The updating of the optimal step-size α_{opt} is obtained as:

$$s = \left(\frac{tol \cdot \alpha}{2|\hat{\mathbf{z}}_i - \mathbf{z}_i|}\right)^{\frac{1}{5}} \quad (16a)$$

$$\alpha_{opt} = s \cdot \alpha \quad (16b)$$

$$\mathbf{z}_i = \mathbf{z}_{i-1} + \frac{35k_1}{384} + \cancel{0k_2} + \frac{500k_3}{1113}\frac{125k_4}{192} - \frac{2187k_5}{6784} + \frac{11k_6}{84} + \cancel{0k_7} \tag{12a}$$

$$\hat{\mathbf{z}}_i = \mathbf{z}_{i-1} + \frac{5179k_1}{57600} + \cancel{0k_2} + \frac{7571k_3}{16695}\frac{393k_4}{640} - \frac{92097k_5}{339200} + \frac{187k_6}{2100} + \frac{k_7}{40} \tag{12b}$$

$$k_1 = \alpha f(t_{i-1}, \mathbf{z}_{i-1}) \tag{12c}$$

$$k_2 = \alpha f\left(t_{i-1} + \frac{\alpha}{5}, \mathbf{z}_{i-1} + \frac{k_1}{5}\right) \tag{12d}$$

$$k_3 = \alpha f\left(t_{i-1} + \frac{3\alpha}{10}, \mathbf{z}_{i-1} + \frac{3k_1}{40} + \frac{9k_2}{40}\right) \tag{12e}$$

$$k_4 = \alpha f\left(t_{i-1} + \frac{4\alpha}{5}, \mathbf{z}_{i-1} + \frac{44k_1}{45} - \frac{56k_2}{15} + \frac{32k_3}{9}\right) \tag{12f}$$

$$k_5 = \alpha f\left(t_{i-1} + \frac{8\alpha}{9}, \mathbf{z}_{i-1} + \frac{19372k_1}{6561} - \frac{25360k_2}{2187} + \frac{64448k_3}{6561} - \frac{212k_4}{729}\right) \tag{12g}$$

$$k_6 = \alpha f\left(t_{i-1} + \alpha, \mathbf{z}_{i-1} + \frac{9017k_1}{3168} - \frac{355k_2}{33} - \frac{46732k_3}{5247} + \frac{49k_4}{176} - \frac{5103k_5}{18656}\right) \tag{12h}$$

$$k_7 = \alpha f\left(t_{i-1} + \alpha, \mathbf{z}_{i-1} + \frac{35k_1}{384} + \cancel{0k_2} + \frac{500k_3}{1113}\frac{125k_4}{192} - \frac{2187k_5}{6784} + \frac{11k_6}{84}\right) \tag{12i}$$

TABLE I
PROPOSED NETWORK TOPOLOGY

Feature extraction network								
	Module ID	**Sub-module**	**Norm.**	**Activation**	**Kernel**	**Stride**	**Padding**	**Pooling**
FE-head	F_1	-	-	-	$64 \times 3 \times 3 \times n_3$	1	-	-
	F_2	Stage 1	Yes (64)	ReLU	$64 \times 3 \times 3 \times 64$	2	Yes	-
		Stage 2	Yes (64)	ReLU	$64 \times 3 \times 3 \times 64$	1	-	-
		Skip connection	-	-	$64 \times 1 \times 1 \times 64$	2	-	-
FE-body	$\mathcal{G}(\cdot)$	Stage 1	Yes (64)	ReLU	$64 \times 3 \times 3 \times 64$	1	Yes	-
		Stage 2	Yes (64)	ReLU	$64 \times 3 \times 3 \times 64$	1	Yes	-
		Stage 3	Yes (64)	-	-	-	-	-
FE-tail	F_3	Stage 1	Yes (64)	ReLU	-	-	-	Average (1×1)

Classification network			
	Layer	**Neurons**	**Activation**
MLP	F_4	64	ReLU
	F_5	$n_{classes}$	Softmax

where tol defines the tolerance level, which provides robustness and reliability to the model.

In addition to obtaining the corresponding state $\mathbf{X}_T = F(t_T)$ at t_T (forward-propagation), the *ODEsolver* should optimize the network's parameters associated to the differential equation $\mathcal{G}(t, F(t), \theta)$ by back-propagating the internal error signal $E_{ode}(\cdot)$, defined by the following expression:

$$E_{ode}(F(t_T)) = E\left(F(t_0) + \int_{t_0}^{t_T} \mathcal{G}\left(t, F(t), \theta\right) dt\right) \tag{17}$$

This optimization can be implemented by two methods: i) traditional integration through a *Runge-Kutta integrator*, for instance, or ii) employing the *adjoint method* [54], [62]. The first one directly integrates the operations of the forward pass and still presents an important memory requirements in the sense that, for $\hat{L}$ evaluations, the memory cost grows to the order of $\mathcal{O}(\hat{L})$. However, the adjoint method allows to optimize the parameters of $\mathcal{G}(\cdot)$ while significantly reducing their management, keeping constant the memory cost in the order $\mathcal{O}(1)$ [54].

Finally, the FE-layers end with the FE-tail, which receives $\mathbf{X}_T$, the estimated output of the *ODEsolver* at evaluation time t_T, and performs a final processing. This entails a FE and detection stage, denoted as F_3, which comprises normalization, nonlinear, and average pooling layers. The obtained feature maps are then reshaped and sent to the classifier, which has been implemented as an MLP with two FC layers: F_4 and F_5, where the last one produces the final classification.

Table I gives the topology details of the proposed ODEnet. Moreover, our ODEnet model has been trained by the Stochastic Gradient Descend (SGD) optimizer to minimize the classification loss given by Eq. (3), with input patches of 11×11, using 160 epochs and 0.1 as learning rate, taking into account a momentum of 0.9 and learning rate decay, and a batch-size of 128, while the *ODEsolver* is implemented via the DOPRI5 solver with a tolerance fixed to $tol = 1e-3$ and an integration time interval of $[0, 1]$, which directly controls the number of evaluations $\hat{L}$ of the model by obtaining the optimal step-size α.

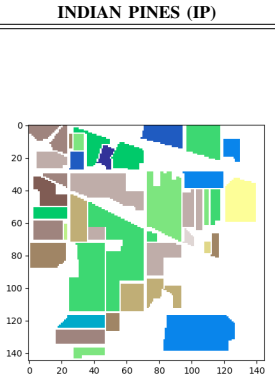

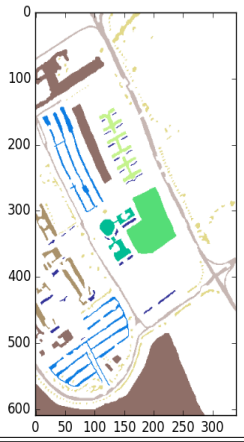

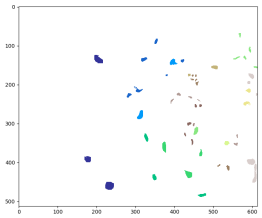

INDIAN PINES (IP)			UNIVERSITY OF PAVIA (UP)			SALINAS VALLEY (SV)			KENNEDY SPACE CENTER (KSC)		
Color	Land-cover type	Samples	Color	Land-cover type	Samples	Color	Land-cover type	Samples	Color	Land-cover type	Samples
	Background	10776		Background	164624		Background	56975		Background	309157
	Alfalfa	46		Asphalt	6631		Brocoli-green-weeds-1	2009		Scrub	761
	Corn-notill	1428		Meadows	18649		Brocoli-green-weeds-2	3726		Willow-swamp	243
	Corn-min	830		Gravel	2099		Fallow	1976		CP-hammock	256
	Corn	237		Trees	3064		Fallow-rough-plow	1394		Slash-pine	252
	Grass/Pasture	483		Painted metal sheets	1345		Fallow-smooth	2678		Oak/Broadleaf	161
	Grass/Trees	730		Bare Soil	5029		Stubble	3959		Hardwood	229
	Grass/pasture-mowed	28		Bitumen	1330		Celery	3579		Swap	105
	Hay-windrowed	478		Self-Blocking Bricks	3682		Grapes-untrained	11271		Graminoid-marsh	431
	Oats	20		Shadows	947		Soil-vinyard-develop	6203		Spartina-marsh	520
	Soybeans-notill	972					Corn-senesced-green-weeds	3278		Cattail-marsh	404
	Soybeans-min	2455					Lettuce-romaine-4wk	1068		Salt-marsh	419
	Soybean-clean	593					Lettuce-romaine-5wk	1927		Mud-flats	503
	Wheat	205					Lettuce-romaine-6wk	916		Water	927
	Woods	1265					Lettuce-romaine-7wk	1070			
	Bldg-Grass-Tree-Drives	386					Vinyard-untrained	7268			
	Stone-steel towers	93					Vinyard-vertical-trellis	1807			
	Total samples	21025		Total samples	207400		Total samples	111104		Total samples	314368

Fig. 3. Number of available labeled samples in the Indian Pines (IP), University of Pavia (UP), Salinas Valley (SV) and Kennedy Space Center (KSC) HSI datasets.

III. Experimental Results

A. Experimental Environment

In order to study the performance of the proposed ODEnet for HSI classification, an implementation has been developed and tested on a hardware environment with a 6th Generation Intel® Core™i7-6700K processor with 8M of Cache and up to 4.20GHz (4 cores/8 way multi-task processing), installed over an ASUS Z170 pro-gaming motherboard. The available memory is 40GB of DDR4 RAM with serial speed of 2400MHz and a Toshiba DT01ACA HDD with 7200RPM and 2TB of storage capacity. Also, a graphic processing unit (GPU) NVIDIA GeForce GTX 1080 with 8GB GDDR5X of video memory and 10 Gbps of memory frequency is available. In order to provide an efficient implementation, the proposed model has been parallelized over the GPU using CUDA 9.0 and cuDNN 7.1.1 language over the Pytorch framework, with Ubuntu 18.04.1 x64 as operating system.

B. Hyperspectral Datasets

Fig. 3 presents the four real HSI datasets that have been considered in our experiments: Indian Pines (IP), Salinas Valley (SV) and Kennedy Space Center (KSC) scenes, acquired by the Airborne Visible/Infrared Imaging Spectrometer (AVIRIS) sensor [63], and the University of Pavia (UP) scene, captured by the Reflective Optics System Imaging Spectrometer (ROSIS) sensor [64]. A detailed description of these images is provided below.

- The IP scene comprises an area with different agricultural fields in Northwestern Indiana, USA, imaged during a flying campaign of the AVIRIS sensor in 1992. The scene contains 145×145 samples, where each one comprises 20 meters, and the spectral information consists of 200 bands in the wavelength range from 0.4 to 2.5 μm, after the removing 24 noisy and corrupted bands. As it can be observed in Fig. 3, the ground-truth of the IP scene contains a total of 16 different classes.
- The UP image was acquired in 2001 by the ROSIS sensor over the University of Pavia, Northern Italy, capturing an urban area of 610×340 pixels, where each one comprises 1.3 meters, and with spectral (103 bands, after elimination of noisy and corrupted bands) in the wavelength range from 0.43 to 0.86 μm. The number of different classes contained in the UP scene is 9.
- The SV image was captured during a flying campaign of the AVIRIS sensor in 1998 over the agricultural area described as Salinas Valley in California, USA. The data comprises 512×217 pixels, with spatial resolution of 3.7 meters per pixel and 200 spectral bands in the range from 0.4 to 2.5 μm (200 bands, after elimination of the

noisiest bands). The available ground-truth for the SV scene contains 16 classes.

- Finally, the KSC scene was also gathered by the AVIRIS instrument in 1996, over the Kennedy Space Center in Florida, USA. In this scene, 512×614 pixels were obtained with spatial resolution of 20 meters per pixel. The data comprises 176 spectral bands in the range range from 0.4 to 2.5 μm, after the removal of noisy bands. The available ground-truth for this scene comprises 13 different classes.

C. Experimental Setting

To evaluate the classification performance of the proposed ODEnet for HSI classification, three widely used quantitative metrics have been considered: the overall accuracy (OA), average accuracy (AA), and Kappa coefficient. Moreover, the number of model's parameters and execution times have also been measured, to determine the volume of data to be trained and the computational cost. In this regard, with the aim of providing a complete and detailed experimentation, several experiments have been carried out:

1) Our first experiment evaluates the performance of the proposed ODEnet by implementing it with different *ODEsolvers*, in particular: forward Euler (EULER), explicit midpoint (MIDPOINT), RK4 and DOPRI5. For this experiment the IP dataset has been considered, selecting randomly 10% of the available labeled samples for training and using the remaining 90% of the samples for testing, setting the tolerance threshold to $tol = 1e{-}3$. Each experiment has been executed 10 times, and the average and standard deviations have been reported.
2) Our second experiment focuses on the DOPRI5 solver, due to its ability to adapt the step-size α, adapting in turn the number of evaluations $\hat{L}$ contained in the defined integration time interval $[t_0, t_T]$ to the complexity of the function, as opposed to the EULER, MIDPOINT and RK4 methods that set a fixed-size for α, making the same number of evaluations in each step. In this regard, our second experiment analyzes the behaviour of the DOPRI5 solver with different tolerance thresholds, in particular: $tol = \{1e\text{-}1,\ 1e\text{-}2,\ 1e\text{-}3\ 1e\text{-}4,\ 1e\text{-}5\}$. For this purpose, the OA values, the number of evaluations during the forward and backward steps, and the training execution times have been measured. Again, in this experiment we randomly select 10% of the available labeled samples of the IP dataset for training and use the remaining 90% for testing. Each experiment is executed 10 times and the average and standard deviations are reported.
3) Once the model's behaviour has been evaluated with different solvers and tolerance levels, our third experiment performs several comparisons between the proposed ODEnet and the traditional ResNet model for spectral-spatial HSI data classification. In this context, this experiment compares the robustness of the models, analyzing their performance based on the amount of available training data, the number of parameters used by each model, and the evolution of the accuracy in each epoch. For a fair comparison, the ResNet has been implemented in the same way as the ODEnet, using the topology in Table I, and changing the *ODEsolver* by six residual units composed by exactly the same stages as the proposed ODEnet's FE-body, but adding the corresponding residual connections. Moreover, the proposed ODEnet has been implemented with the DOPRI5 solver, employing Runge-Kutta integration and adjoint methods and a tolerance threshold of $1e$-3. These models have been tested with all the available scenes. For the IP and KSC scenes, we have randomly selected 5%, 10% and 15% of the available labeled samples for training and used the remaining samples for testing. The fact that we consider larger training percentages for these two images is due to the low spatial resolution and highly mixed nature of these scenes, which exhibit high intra-class variability. In turn, for the UP and SV scenes (which exhibit much larger spatial resolution), we have randomly selected 1%, 5% and 10% of the available labeled samples for training, using the remaining samples for testing. In all cases, we have executed each experiment 10 times and the average and standard deviations are reported.
4) The fourth experiment compares the behaviour of the proposed ODEnet models and the ResNet depending on different network configurations. In particular, the spatial windows size of the network's input data and the depth of the convolutional filters. In this sense, the proposed models have been implemented with DOPRI5 during the forward pass, while employing both Runge-Kutta integrator and the adjoint method during the backward step. For each experiment, the 10% of IP and KSC and the 5% of UP and SV datasets have been considered to perform the training of the models.
   Regarding to the first experiment, it compares the performance of the neural models when different amounts of spatial information conform the network's input data. In this context, different windows sizes have been considered, in particular input patches of 5×5, 7×7, 9×9, 11×11, 13×13 and 15×15 pixels have been tested. Separately, the second experiment compares the networks' behaviour when the number of convolutional filters grows. In this regard, convolutional layers have been implemented with 8, 16, 32, 64 and 128 filters.
5) Our last experiment conducts a comparison of the proposed ODEnet with other widely used HSI classifiers. In this context, eight different classification methods have been selected to conduct the experimental validation. Specifically, three pixel-wise classifiers (MLR, SVM with radial basis function kernel and MLP), one deep spatial classifier (CNN2D) and four spectral-spatial deep architectures (CNN3D, ResNet and the proposed ODEnet) have been considered. In this experiment, we have randomly selected 15% of the available labeled data from the IP and KSC scenes, and used the remaining 85% of the labeled data for testing. Considering the higher spatial resolution of the UP and SV scenes, we

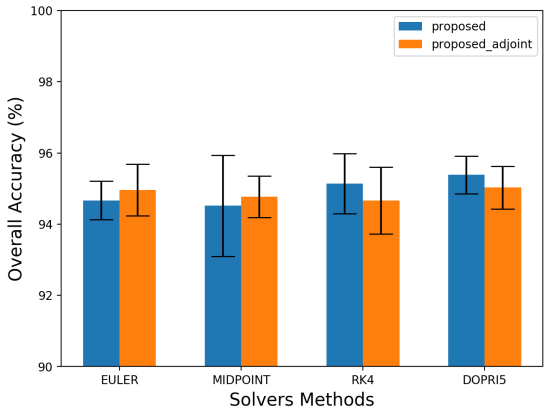

Fig. 4. Overall accuracy values (and corresponding standard deviations) obtained by the proposed method (implemented with four different solvers with Runge-Kutta integration and adjoint methods) for the IP scene.

have randonly selected 10% of the available labeled samples for these scenes, and used the remaining 90% for testing. As in previous experiments, we repeated each experiment 10 times and report the average and standard deviations. Moreover, for the spatial (CNN2D) and the spectral-spatial (CNN3D, ResNet, and ODEnet) methods, the original HSI scene has been cropped into patches of 11×11. In the case of the CNN2D, principal component analysis (PCA) has been used to reduce the number of spectral bands to a single principal component. All the hyperparameters of the considered methods have been optimally fixed to obtain the best possible performance for each method.

D. Experiment 1: testing different ODEsolvers

The performance of the proposed ODEnet depends on two main aspects: i) the solver that performs the forward evaluation, and ii) the backpropagation method that implements the reverse-mode differentiation. In this experiment, the fixed-α solvers: EULER, MIDPOINT and RK4, and the adaptive solver: DOPRI5 have been compared using the IP dataset, testing each one with Runge-Kutta integration (simply referred to ODEnet hereinafter) and the adjoint method (ODEnetAdj hereinafter).

Fig. 4 gives the obtained OA results and the standard deviations for each considered model. As a general comment, it should be noted that all methods achieve an OA greater than 94%, with small differences between them. Specifically, the difference between the implementation of each solver with Runge-Kutta integration and adjoint method is very small, achieving very similar results.

If we compare the fixed-α solvers (EULER, MIDPOINT and RK4) with the adaptive DOPRI5 solver, it can be observed that DOPRI5 reaches the best OA values for both backpropagation methods, Runge-Kutta integration and adjoint, exceeding 95% OA with very low standard deviation, due to its capability of adapting the evaluations to the problem's complexity. Furthermore, MIDPOINT and RK4 exhibit the worse OA scores when implemented using Runge-Kutta integration and adjoint methods, respectively. In particular, the MIDPOINT method implemented with Runge-Kutta integration exhibits the highest standard deviation, because the adopted approximation strategy performed by calculating the midpoint of the slope is not the most approapriate for complex data such as HSI scenes.

E. Experiment 2: testing different tolerance thresholds for DOPRI5 solver

The DOPRI5 solver is able to adapt the step-size α that controls the number of evaluation points ($\hat{L}$) carried out inside the integration time interval $[t_0, t_T]$, providing a flexible mechanism to adapt the ODE resolution to the complexity of the considered HSI data. In this sense, five different values for the tolerance threshold have been considered: {$1e$-1, $1e$-2, $1e$-3 $1e$-4, $1e$-5}.

Fig. 5 shows the obtained results, comparing the obtained OA values [see Fig. 5(a)], the training runtimes [see Fig. 5(b)], and the number of evaluations performed during the forward and backward steps (for each tolerance value) [see Fig. 5(c)]. If we focus on Fig. 5(a), it can be observed that the tolerance threshold does not have a relevant impact on the OA values, in the sense that the differences are very small and the slight variations are mainly due to the random procedure used for the selection of training samples.

However, if we focus on [see Fig. 5(b)] it can be clearly observed that, for lower tolerances, the execution times gradually increase, being the implementations with DOPRI5 and adjoint method the slowest ones. This is due to the number of evaluations $\hat{L}$ that need to be carried out, both in the forward evaluations and in the backward propagation. To further investigate this issue, Fig. 5(c)] focuses on the DOPRI5 solver implementation with the adjoint method. In general, the number of forward and backward evaluations in this case is high in the early epochs, with the aim of adjusting them to minimize the approximation error, descending abruptly until the number becomes stable in subsequent epochs. In addition, for lower tolerances it can be observed that the number of evaluations is higher than for tolerance values of $1e$-1 and $1e$-2, where the difference is minimal. With the aforementioned observations in mind, we consider a tolerance of $1e$-3 as a good choice, in the sense that it provides a good balance between performance and training times, together with a sufficiently high number of evaluations.

F. Experiment 3: comparing ODEnet with ResNet

In this experiment we illustrate the benefit of implementing a ResNet-inspired model as a continuous function defined by an ODE. Fig. 6 shows the OA evolution of the proposed ODEnet when different amounts of training samples are available. In general, the proposed method, implemented either with DOPRI5 and Runge-Kutta integrator (ODEnet) or with the adjoint method (ODEnetAdj) exhibits the best OA results for all the considered HSI scenes, regardless of the training percentage employed. The differences between our ODEnet/ODEnetAdj models and the ResNet become particularly evident when very few training samples are available,

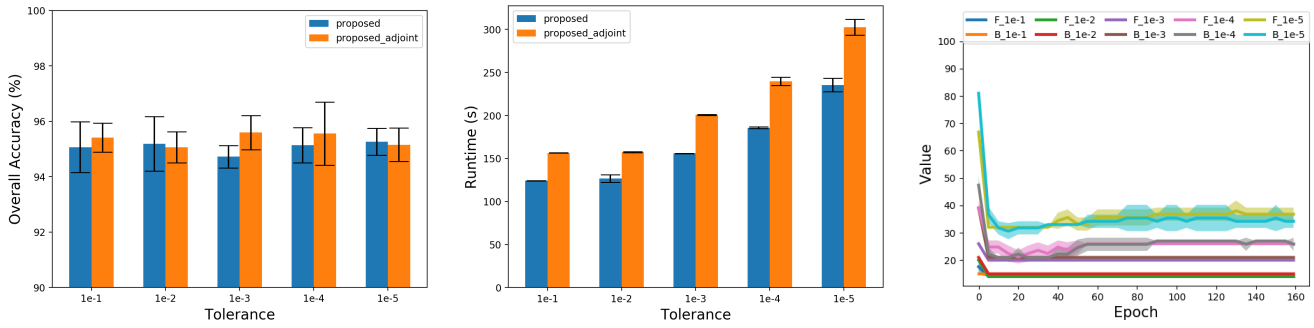

(a) (b) (c)

Fig. 5. Performance of ODEnet (on the IP scene) with the DOPRI5 solver, using Runge-Kutta integration and adjoint methods, considering different tolerance values. Specifically, we analyze the impact on the overall accuracy (a), the training runtimes (b), and the number of evaluations per epoch (c) during the forward and backward steps of the DOPRI5 solver implemented with the adjoint method.

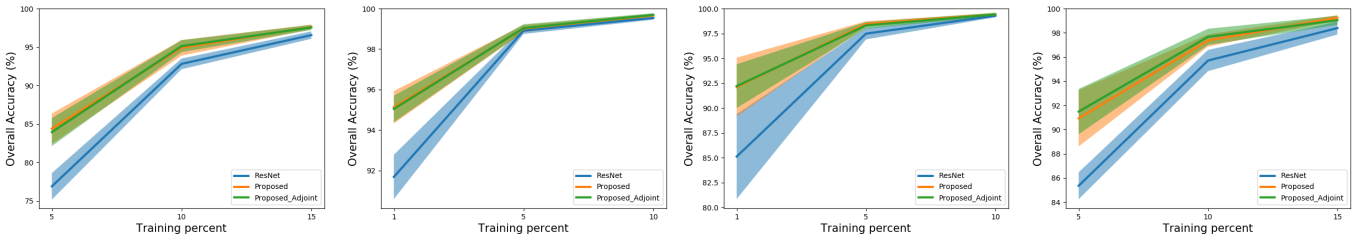

(a) (b) (c) (d)

Fig. 6. Evolution of the overall accuracy reached by ResNet (blue), the proposed ODEnet with DOPRI5 solver and Runge-Kutta integration (orange), and the proposed ODEnet with DOPRI5 solver and adjoint method (green), considering different amounts of training data. We report the results obtained for the IP (a), UP (b), SV (c) and KSC (d) scenes.

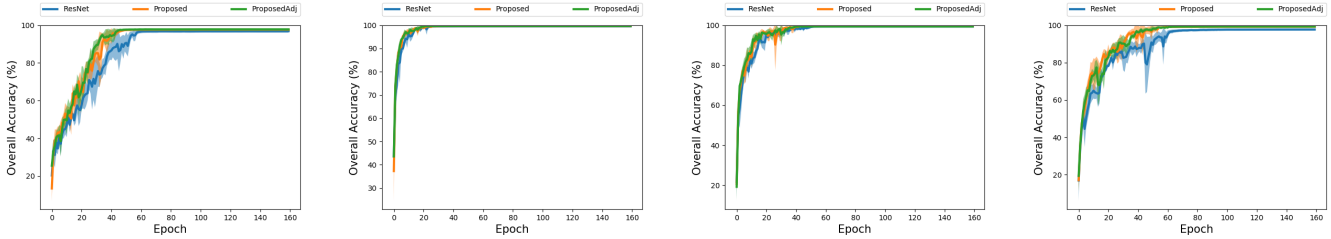

(a) (b) (c) (d)

Fig. 7. Evolution of the overall accuracy reached by ResNet (blue), the proposed ODEnet with DOPRI5 solver and Runge-Kutta integration (orange), and the proposed ODEnet with DOPRI5 solver and adjoint method (green) at different epochs. We report the results obtained for the IP (a), UP (b), SV (c) and KSC (d) scenes.

with the proposed models exhibiting the most robust results. Again, the observable differences between the Runge-Kutta integrator and the adjoint method are quite small, being the adjoint method better for KSC and SV scenes with low training percentages.

The aforementioned results clearly illustrate the impact that the overfitting of learnable parameters has on the ResNet model, which needs more training data to achieve the same performance as our ODEnet models. Moreover, Fig. 7 illustrates that this overfitting problem happens at early epochs of the classifiers. Specifically, it can be observed in this figure how the OA obtained by ODEnet inceases faster than that achieved by ResNet in the earliest epochs, in particular when complex scenes (such as IP and KSC) are classified.

These observed benefits confirm the following introspections: the ability of the DOPRI5 solver to adapt the model's learning to the complexity of the problem, and the significant reduction that can be achieved in terms of the required number of parameters. The latter important benefit is quantitatively measured in Table II, where the number of required model parameters are displayed for each HSI dataset. Specifically, the proposed ODEnet and ODEnetAdj models are able to overcome the performance of the traditional ResNet model by using less than half of its training parameters, avoiding quite

TABLE II
NUMBER OF TRAINABLE PARAMETERS FOR THE STANDARD RESNET MODEL AND THE PROPOSED METHOD, IMPLEMENTED WITH DOPRI5 SOLVER AND RUNGE-KUTTA INTEGRATION (ODENET), AND WITH THE ADJOINT METHOD (ODENETADJ).

Dataset	ResNet	ODEnet	ODEnetAdj	Reduction
IP	638416	268624	268624	2.38
UP	582089	212297	212297	2.74
SV	640720	270928	270928	2.36
KSC	624397	254605	254605	2.45

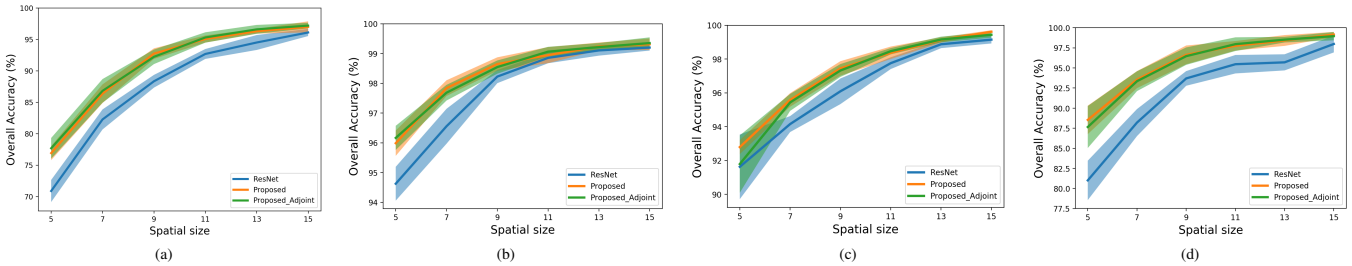

Fig. 8. Evolution of the overall accuracy reached by ResNet (blue), the proposed ODEnet with DOPRI5 solver and Runge-Kutta integration (orange), and the proposed ODEnet with DOPRI5 solver and adjoint method (green), considering different spatial windows size. We report the results obtained for the IP (a), UP (b), SV (c) and KSC (d) scenes.

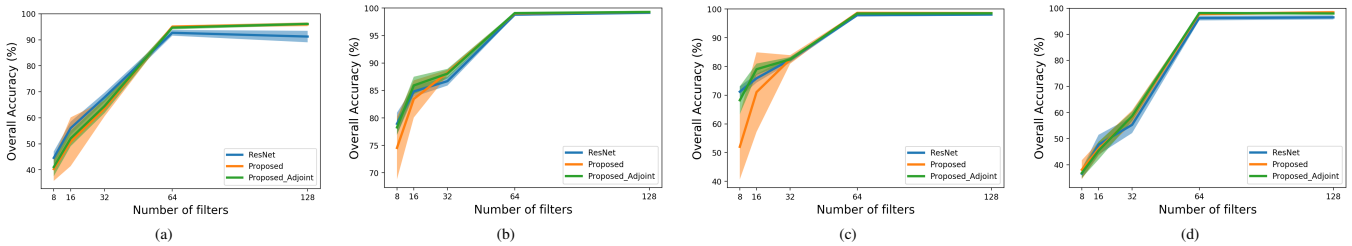

Fig. 9. Evolution of the overall accuracy reached by ResNet (blue), the proposed ODEnet with DOPRI5 solver and Runge-Kutta integration (orange), and the proposed ODEnet with DOPRI5 solver and adjoint method (green), considering different number of filters in each block. We report the results obtained for the IP (a), UP (b), SV (c) and KSC (d) scenes.

effectively the overfitting problem.

G. Experiment 4: testing different network configurations

In this experiment, we report the results obtained by the proposed ODEnet considering different configurations of the model, in particular the initial amount of information employed by the ODEnet, ODEnetAdj and ResNet by testing different spatial sizes of the models' input data-patch, and the number of features extracted and processed by the convolutional layers.

On the one hand, Fig. 8 shows the obtained results in terms of OA considering input patches composed by 5×5, 7×7, 9×9, 11×11, 13×13 and 15×15 pixels. As we can observe, the proposed models exhibit very similar behaviours, being able to outperform the accuracy reached by the ResNet in every scene, in particular when the spatial windows are very small. Moreover, the improvement in the OA's values increases as the spatial windows size increases. However, while the difference, in terms of accuracy, between small spatial windows is very pronounced (for instance, between windows of 5×5 and 9×9 pixels, there are approximately 10 percentage points of improvement in IP and KSC, and 4 percentage points in UP and SV), between bigger windows the difference is noticeably smaller (for instance, between windows of 11×11 and 15×15). In this sense, as the amount of information to be processed increases with the dimensions of the input data-patch, increasing also both memory requirements and computation times, we consider pathes of 11×11 pixels as an optimal input data size, with a good ratio between performance and computing time.

On the other hand, Fig. 9 shows the obtained results in terms of OA too, considering input patches of 11×11 and convolutional layers with 8, 16, 32, 64 and 128 filters. As we can observe for each dataset, the OA increases its value as more filters are added. In particular, the best OA is reached with 64 filters, remaining quite similar with 128 filters. Actually, the OA is improved very slightly with 128 filters, however the computational cost of this network's configuration is considerably higher than with 64 filters. For this reason we consider 64 to be the optimum number of filters for each convolutional layer.

H. Experiment 5: testing different HSI classifiers

Our final experiment compares our proposed ODEnet models with some widely-used classifiers available in the HSI classification literature. Figs. 10 (IP), 11 (UP), 12 (SV) and 13 (KSC) show the classification maps obtained by each considered method, while Tables III (IP), IV (UP), V (SV) and VI (KSC) give the individual class accuracies and the global OA, AA and Kappa values obtained by each classifier with the corresponding standard deviations, respectively, including also the obtained runtimes of each experiment.

As a general comment, the improvement introduced by spatial and spectral-spatial models over pixel-wise classifiers is remarkable. For instance, CNN2D introduces around 2% points of improvement in OA when compared to the most accurate spectral model, i.e. the SVM (for UP and SV) and the MLP (for IP), with an exception in the KSC scene, in which the spatial information appears to be not enough discriminatory enough to carry out an accurate classification, as we can observe on Table VI and the corresponding classification maps on Fig. 13. The limitations of pixel-wise and spatial-based classifiers can be easily overcome by spectral-spatial classifiers, where the combination of spectral and spatial-contextual information is able to significantly reduce the uncertainty and data variability of HSI pixels, as it can

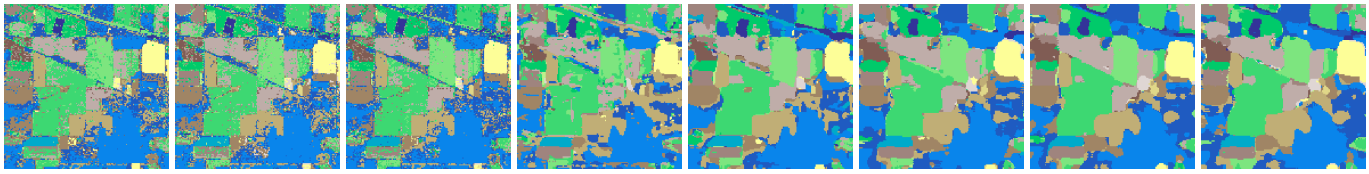

a) MLR (78.19%) *b*) SVM (83.63%) *c*) MLP (84.03%) *d*) CNN2D (87.16%) *e*) CNN3D (95.45%) *f*) ResNet (96.55%) *g*) **ODEnet (97.61%)** *h*) ODEnetAdj (97.55%)

Fig. 10. Classification maps obtained for the IP scene by different classifiers (see Table III). Note that the overall classification accuracies are shown in brackets and the best result is highlighted in bold font.

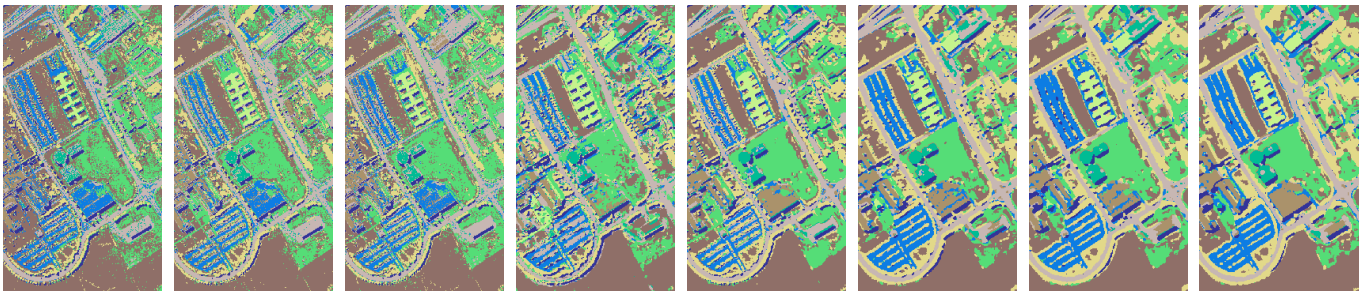

a) MLR (89.89%) *b*) SVM (94.40%) *c*) MLP (94.39%) *d*) CNN2D (96.02%) *e*) CNN3D (99.02%) *f*) ResNet (99.54%) *g*) ODEnet (99.67%) ***h*) ODEnetAdj (99.69%)**

Fig. 11. Classification maps obtained for the UP scene by different classifiers (see Table IV). Note that the overall classification accuracies are shown in brackets and the best result is highlighted in bold font.

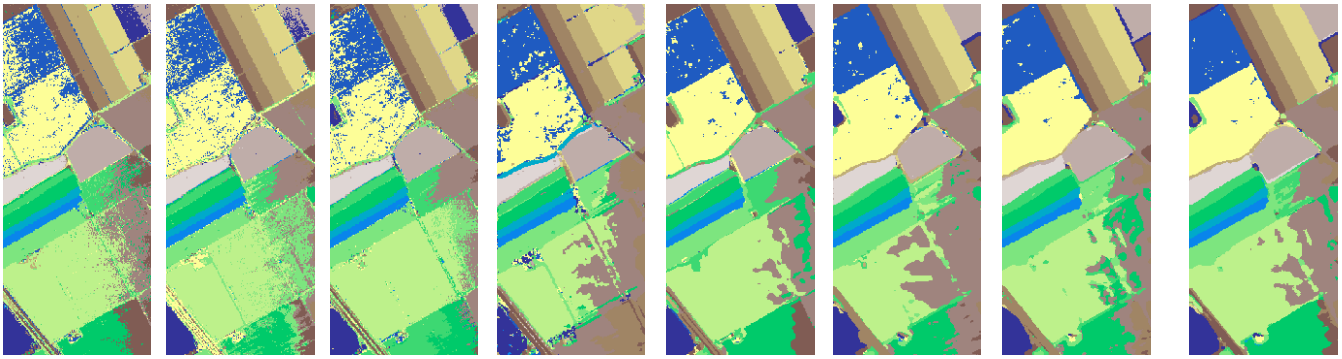

a) MLR (92.37%) *b*) SVM (93.65%) *c*) MLP (93.15%) *d*) CNN2D (95.27%) *e*) CNN3D (98.45%) *f*) ResNet (99.28%) *g*) **ODEnet (99.42%)** *h*) ODEnetAdj (99.41%)

Fig. 12. Classification maps obtained for the SV scene by different classifiers (see Table V). Note that the overall classification accuracies are shown in brackets and the best result is highlighted in bold font.

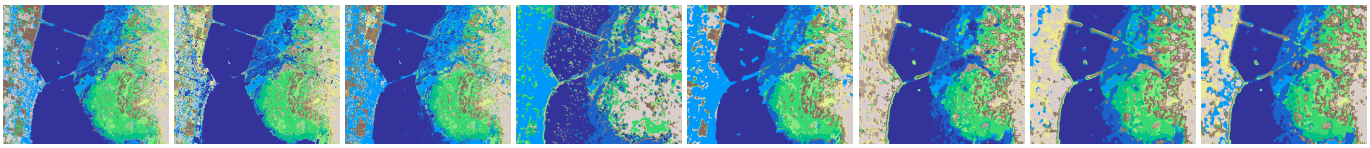

a) MLR (92.74%) *b*) SVM (92.92%) *c*) MLP (90.22%) *d*) CNN2D (66.04%) *e*) CNN3D (98.10%) *f*) ResNet (98.39%) *g*) **ODEnet (99.24%)** *h*) ODEnetAdj (99.03%)

Fig. 13. Classification maps obtained for the KSC scene by different classifiers (see Table VI). Note that the overall classification accuracies are shown in brackets and the best result is highlighted in bold font.

be observed on complex datasets such as IP (see Table III) and, particularly, KSC (see Table VI). This results in better classification maps, where the "salt & pepper" classification noise is practically removed. However, it is interesting to focus on the classification maps produced by the spatial-spectral CNN3D classifier (for instance in Figs. 11 and 13), where multiple patches has been wrongly labelled, obtaining visually noisy classification maps. This can be observed in the lower-leftmost corner of the KSC scene (see Fig. 13), where the vast majority of pixels have been miss-classified as Salt-marsh. These deficiencies are highlighted by the differences between the OA and AA values, where the AA is several percentual points lower, indicating the existence of an overfitting problem (see Tables III and VI).

Adding residual learning via ResNet can improve the accuracy results, reducing the gap between the OA and AA on some HSI datasets such as UP (see Table IV), SV (see Table V) and KSC (see Table VI), and improving the visual appearence of the corresponding classification maps. However, this gap between the OA and AA scores cannot be reduced by ResNet in the IP scene (in fact, for this scene the gap becomes larger). In turn, the proposed ODEnet models are able to reach very similar OA, AA and Kappa values in all cases, exhibiting very good consistency in terms of model

TABLE III
CLASSIFICATION RESULTS OBTAINED BY DIFFERENT METHODS FOR THE IP DATASET, USING 15% OF THE AVAILABLE LABELED DATA FOR TRAINING AND 11×11 INPUT SPATIAL PATCH SIZE.

Class	MLR	SVM	MLP	CNN2D	CNN3D	ResNet	ODEnet	ODEnetAdj
0	74.59±0.48	81.36±0.42	81.23±0.96	85.61±1.09	95.34±0.72	96.07±0.55	**97.28**±0.34	97.21±0.38
1	33.33±10.51	56.92±12.96	65.38±13.96	75.38±17.7	80.77±15.44	86.41±9.87	93.08±5.13	**93.59**±5.29
2	76.36±1.9	81.12±1.09	78.92±2.09	84.63±2.56	94.68±1.84	94.15±1.02	96.02±1.43	**96.08**±0.97
3	57.3±2.15	74.03±2.01	68.14±3.81	77.63±3.52	95.32±1.44	94.4±2.79	**97.15**±1.44	97.09±1.69
4	43.03±6.83	61.29±4.81	73.78±4.65	84.13±5.09	91.84±3.68	**96.77**±2.48	96.62±2.61	96.32±2.72
5	86.73±3.94	89.71±3.83	88.46±2.8	83.29±5.47	96.15±2.07	97.24±1.21	96.63±1.7	**97.63**±2.86
6	96.23±0.9	97.0±1.13	95.13±1.66	90.47±2.48	99.11±0.47	97.71±1.08	**99.18**±0.38	98.76±0.59
7	54.78±7.33	77.39±10.07	82.61±7.78	84.78±16.53	80.87±17.95	80.87±12.17	96.52±5.43	**96.96**±4.37
8	98.45±0.96	97.73±1.87	98.69±1.13	97.17±2.27	99.73±0.58	99.43±1.09	**99.9**±0.16	99.9±0.16
9	18.24±13.27	50.59±11.22	64.71±13.67	**85.88**±11.53	83.53±17.41	67.65±18.27	82.94±10.0	77.65±9.41
10	65.3±2.2	76.42±1.97	78.98±3.67	78.75±3.78	94.49±2.55	95.33±1.79	**97.53**±1.35	96.38±1.46
11	79.87±1.71	84.21±1.65	83.25±2.19	90.48±1.53	96.87±1.19	97.77±0.72	98.23±0.47	**98.26**±0.43
12	61.23±2.31	77.64±2.14	79.58±4.16	76.25±3.54	89.48±4.18	94.01±1.81	94.11±2.46	**95.32**±1.49
13	98.51±0.64	98.33±1.13	98.1±1.06	98.33±1.13	**99.89**±0.23	99.54±0.5	99.25±0.85	99.6±0.45
14	94.99±1.31	94.51±1.71	95.79±0.92	97.4±0.95	98.91±0.47	99.09±0.87	99.23±1.07	**99.29**±0.7
15	63.2±3.62	62.93±4.7	65.88±3.48	89.7±3.71	91.68±4.25	97.13±2.58	**97.65**±1.45	96.55±2.62
16	86.08±2.59	87.47±4.22	94.05±4.57	93.42±5.39	**98.48**±2.18	93.92±5.18	96.84±3.93	95.7±3.81
OA (%)	77.87±0.42	83.68±0.38	83.57±0.85	87.43±0.95	95.92±0.63	96.55±0.48	**97.61**±0.3	97.55±0.33
AA (%)	69.6±0.59	79.21±1.49	81.97±1.76	86.73±1.91	93.24±1.61	93.21±1.45	**96.3**±0.87	95.94±1.09
Kappa (x100)	74.59±0.48	81.36±0.42	81.23±0.96	85.61±1.09	95.34±0.72	96.07±0.55	**97.28**±0.34	97.21±0.38
Runtime (s)	5.99±1.03	**0.28**±0.01	99.49±5.46	66.55±4.16	172.89±15.73	81.63±0.13	192.6±0.19	257.55±2.62

TABLE IV
CLASSIFICATION RESULTS OBTAINED BY DIFFERENT METHODS FOR THE UP DATASET, USING 10% OF THE AVAILABLE LABELED DATA FOR TRAINING AND 11×11 INPUT SPATIAL PATCH SIZE.

Class	MLR	SVM	MLP	CNN2D	CNN3D	ResNet	ODEnet	ODEnetAdj
0	86.42±0.2	92.56±0.14	92.42±0.25	94.72±0.29	99.08±0.13	99.39±0.11	99.56±0.1	**99.59**±0.11
1	92.31±0.62	94.46±0.58	94.98±0.72	95.12±0.99	99.19±0.38	99.44±0.25	**99.64**±0.17	99.59±0.3
2	96.07±0.36	98.31±0.18	97.82±0.3	98.21±0.33	99.89±0.06	99.87±0.09	**99.93**±0.06	99.89±0.05
3	74.0±1.86	79.37±1.84	80.32±2.92	90.33±1.45	96.88±0.79	98.3±1.18	98.89±0.52	**99.08**±0.65
4	88.49±0.96	94.55±0.58	93.59±1.65	97.6±0.54	99.18±0.39	**99.23**±0.38	99.22±0.38	99.13±0.44
5	99.31±0.27	99.28±0.18	99.54±0.15	99.16±0.49	**100.0**±0.0	99.98±0.05	99.98±0.05	99.98±0.05
6	77.42±0.84	88.86±1.06	89.93±1.62	92.01±0.96	**99.88**±0.14	99.62±0.37	99.82±0.18	99.87±0.22
7	57.03±3.04	85.41±2.02	85.98±1.94	83.54±3.16	93.85±2.17	98.08±0.74	98.48±1.2	**98.77**±1.04
8	86.77±0.76	90.67±1.11	89.43±1.83	96.63±0.77	98.84±0.24	99.37±0.38	99.4±0.36	**99.65**±0.24
9	99.77±0.1	**99.91**±0.1	99.89±0.1	98.92±0.87	99.82±0.18	98.98±1.1	99.33±0.75	99.72±0.24
OA (%)	89.84±0.16	94.41±0.1	94.3±0.19	96.02±0.22	99.31±0.1	99.54±0.08	99.67±0.08	**99.69**±0.08
AA (%)	85.69±0.33	92.31±0.24	92.39±0.37	94.61±0.47	98.62±0.26	99.21±0.19	99.41±0.22	**99.52**±0.1
Kappa (x100)	86.42±0.2	92.56±0.14	92.42±0.25	94.72±0.29	99.08±0.13	99.39±0.11	99.56±0.1	**99.59**±0.11
Runtime (s)	9.11±1.57	0.4±0.01	439.55±22.77	306.69±19.04	409.88±65.98	160.17±0.43	508.68±1.71	671.88±3.54

performance, with higher robustness on the obtained results. As we can observe, the proposed method is able to reach the best accuracy scores in all the considered datasets, visually clean classification maps, where the number of miss-classified patches is drastically reduced.

If we now focus on the execution times reported on Tables III (IP), IV (UP), V (SV) and VI (KSC), it can be observed that pixel-wise methods are faster than spatial and spectral-spatial ones, being SVM the fastest classifier. The computational cost of the proposed ODEnet model is higher when compared to the other deep models (CNN2D, CNN3D and ResNet), mainly due to the great optimization performed by the frameworks in which these classifiers have been implemented. In this regard, it is necessary to conduct an effort to optimize the code of the *ODEsolver* in order to provide a more efficient version, although (as shown in our second experiment), the use of higher tolerance values allows for a significant reduction of computation times.

IV. CONCLUSIONS AND FUTURE LINES

This work proposes, for the first time in the literature, a redefinition of the traditional discrete-layer ResNet model as a continuous-time evolving model through the implementation of an ODE parameterized by a neural network, with the aim of improving the classification of remotely sensed HSI data by producing better and more robust feature representations.

The obtained experimental results, conducted using four widely-used HSI datasets, demonstrate the significant benefits and improvements introduced by the proposed method, which is able to reach consistently higher accuracy values in comparison with the traditional ResNet model, at the same time that it significantly reduces the number of parameters that need to be used and fine-tuned, providing a highly efficient mechanism to address the problems of overfitting and data degradation in very deep networks. Moreover, the integration of adaptive solvers such as DOPRI5 offers great flexibility when processing and classifying complex HSI scenes, allowing the model to obtained highly refined features for classification purposes.

TABLE V
CLASSIFICATION RESULTS OBTAINED BY DIFFERENT METHODS FOR THE SV DATASET, USING 10% OF THE AVAILABLE LABELED DATA FOR TRAINING AND 11×11 INPUT SPATIAL PATCH SIZE.

Class	MLR	SVM	MLP	CNN2D	CNN3D	ResNet	ODEnet	ODEnetAdj
0	91.55±0.11	92.94±0.16	92.37±0.17	94.72±0.49	98.23±0.21	99.2±0.18	**99.35**±0.16	99.35±0.19
1	99.49±0.24	99.57±0.28	99.52±0.37	97.2±2.3	**100.0**±0.0	99.84±0.24	99.91±0.1	99.91±0.1
2	99.92±0.06	99.79±0.13	99.89±0.11	98.96±1.04	**99.98**±0.04	99.91±0.13	99.86±0.21	99.88±0.19
3	99.45±0.25	99.58±0.16	99.15±0.51	96.66±3.15	**99.94**±0.07	99.85±0.14	99.91±0.17	99.8±0.25
4	99.25±0.21	99.3±0.38	99.31±0.34	99.79±0.39	99.67±0.28	99.44±0.62	99.68±0.43	**99.83**±0.17
5	99.07±0.23	98.69±0.47	99.13±0.26	98.75±1.29	99.24±0.38	**99.86**±0.16	99.83±0.25	99.85±0.16
6	99.94±0.05	99.85±0.09	99.86±0.14	99.35±0.46	100.0±0.01	**100.0**±0.0	100.0±0.0	100.0±0.01
7	99.68±0.17	99.71±0.16	99.62±0.25	99.51±0.36	99.74±0.28	99.88±0.11	**99.97**±0.05	99.92±0.11
8	87.57±0.6	88.38±0.63	87.1±1.06	92.47±1.43	96.54±0.5	98.42±0.39	**98.82**±0.38	98.62±0.41
9	99.8±0.15	99.72±0.13	99.87±0.17	99.13±0.44	99.96±0.08	**99.98**±0.02	99.96±0.07	99.96±0.04
10	95.41±0.88	96.16±0.71	96.34±0.81	96.66±1.03	99.19±0.34	99.59±0.25	**99.75**±0.32	99.48±0.64
11	97.54±0.91	97.8±0.81	98.3±1.65	97.64±1.14	99.56±0.23	**99.84**±0.31	99.69±0.51	99.4±0.48
12	99.68±0.2	99.74±0.21	99.73±0.16	97.76±1.41	**100.0**±0.0	99.97±0.07	99.99±0.02	99.99±0.02
13	99.14±0.4	98.68±0.68	98.39±1.37	98.68±0.77	99.65±0.79	99.58±0.6	99.62±0.54	**99.82**±0.29
14	96.87±1.07	96.23±1.87	96.81±1.41	97.65±1.18	99.17±0.64	99.69±0.41	**99.89**±0.28	99.85±0.19
15	67.47±0.57	75.4±1.08	73.2±2.13	85.05±2.24	94.79±1.13	97.91±0.67	98.08±0.47	**98.49**±0.73
16	98.64±0.42	98.76±0.37	98.79±0.43	93.37±1.94	99.51±0.35	99.58±0.45	**99.79**±0.18	99.76±0.19
OA (%)	92.42±0.1	93.66±0.14	93.15±0.15	95.26±0.44	98.41±0.19	99.28±0.16	**99.42**±0.14	99.41±0.18
AA (%)	96.18±0.08	96.71±0.09	96.56±0.18	96.79±0.24	99.18±0.1	99.58±0.12	**99.67**±0.09	99.66±0.09
Kappa (x100)	91.55±0.11	92.94±0.16	92.37±0.17	94.72±0.49	98.23±0.21	99.2±0.18	**99.35**±0.16	99.35±0.19
Runtime (s)	50.49±0.22	1.3±0.02	689.03±29.61	457.91±12.95	826.38±58.19	239.64±0.18	730.73±36.55	972.9±36.21

TABLE VI
CLASSIFICATION RESULTS OBTAINED BY DIFFERENT METHODS FOR THE KSC DATASET, USING 15% OF THE AVAILABLE LABELED DATA FOR TRAINING AND 11×11 INPUT SPATIAL PATCH SIZE.

Class	MLR	SVM	MLP	CNN2D	CNN3D	ResNet	ODEnet	ODEnetAdj
0	91.57±0.76	92.52±0.57	88.87±0.55	61.8±1.35	98.22±0.27	98.2±0.59	**99.16**±0.24	98.93±0.42
1	95.0±0.96	95.57±1.31	96.53±0.98	96.35±1.93	**100.0**±0.0	99.47±0.82	100.0±0.0	99.83±0.26
2	93.01±2.24	91.55±3.06	84.76±2.08	37.23±6.03	95.78±2.86	96.7±2.74	98.93±1.55	**99.22**±0.66
3	88.99±1.73	88.89±3.52	88.06±3.62	21.15±8.09	97.37±1.6	96.31±3.35	**99.12**±1.33	96.59±3.74
4	71.17±5.63	74.91±4.73	60.84±5.86	21.26±7.13	86.4±3.18	88.79±2.1	**95.09**±1.91	94.49±4.34
5	71.1±6.49	73.75±4.89	59.56±5.35	57.87±5.07	90.0±4.45	91.99±8.4	90.51±5.11	**92.06**±5.44
6	70.77±7.17	74.79±4.34	58.09±2.73	40.26±14.57	96.6±2.14	98.2±1.09	**98.92**±1.41	98.81±1.56
7	81.57±5.8	86.18±5.1	84.04±4.71	30.79±29.78	99.21±1.33	97.87±2.22	**99.89**±0.34	99.33±1.68
8	91.72±1.84	92.76±2.49	88.5±0.87	35.41±4.06	98.93±1.22	98.91±1.05	99.73±0.35	**99.86**±0.18
9	96.54±1.18	96.92±1.54	96.04±1.43	71.0±4.87	**99.91**±0.21	99.32±0.93	99.59±0.38	99.68±0.61
10	96.27±1.52	97.32±1.91	93.62±1.91	52.94±5.82	99.85±0.44	99.62±0.39	**99.91**±0.19	99.56±1.04
11	97.58±0.92	96.99±2.22	96.99±1.24	95.28±2.07	**99.97**±0.08	99.89±0.34	99.92±0.25	99.55±0.69
12	94.54±3.19	96.21±1.31	92.22±1.16	61.45±6.42	99.65±0.42	99.02±1.17	**99.93**±0.15	99.51±0.74
13	**100.0**±0.0	100.0±0.0	99.72±0.34	91.39±3.37	100.0±0.0	100.0±0.0	100.0±0.0	100.0±0.0
OA (%)	92.43±0.68	93.29±0.51	90.02±0.5	66.03±1.23	98.4±0.24	98.39±0.53	**99.24**±0.21	99.03±0.37
AA (%)	88.33±1.0	89.68±0.87	84.54±0.87	54.8±2.42	97.21±0.48	97.39±0.93	**98.58**±0.49	98.35±0.71
Kappa (x100)	91.57±0.76	92.52±0.57	88.87±0.55	61.8±1.35	98.22±0.27	98.2±0.59	**99.16**±0.24	98.93±0.42
Runtime (s)	2.89±0.24	0.05±0.01	87.98±3.74	66.91±4.63	73.17±1.36	57.47±0.08	114.57±0.17	154.55±7.2

Encouraged by the good results obtained in terms of model's accuracy, in the future we will develop an optimized and parallelized implementation of the proposed ODEnet, exploring other solver algorithms in order to reduce the computational complexity.

ACKNOWLEDGEMENT

The authors would like to thank the Associate Editor and the three anonymous reviewers for their outstanding comments and suggestions, which greatly helped us to improve the technical quality and presentation of this paper.

REFERENCES

[1] J. A. Richards and J. Richards, *Remote sensing digital image analysis*. Springer, 1999, vol. 3.

[2] X.-L. Chen, H.-M. Zhao, P.-X. Li, and Z.-Y. Yin, "Remote sensing image-based analysis of the relationship between urban heat island and land use/cover changes," *Remote sensing of environment*, vol. 104, no. 2, pp. 133–146, 2006.

[3] D. A. Mariano, C. A. dos Santos, B. D. Wardlow, M. C. Anderson, A. V. Schiltmeyer, T. Tadesse, and M. D. Svoboda, "Use of remote sensing indicators to assess effects of drought and human-induced land degradation on ecosystem health in northeastern brazil," *Remote Sensing of Environment*, vol. 213, pp. 129–143, 2018.

[4] T. Lillesand, R. W. Kiefer, and J. Chipman, *Remote sensing and image interpretation*. John Wiley & Sons, 2014.

[5] R. O. Green, M. L. Eastwood, C. M. Sarture, T. G. Chrien, M. Aronsson, B. J. Chippendale, J. A. Faust, B. E. Pavri, C. J. Chovit, M. Solis *et al.*, "Imaging spectroscopy and the airborne visible/infrared imaging spectrometer (aviris)," *Remote sensing of environment*, vol. 65, no. 3, pp. 227–248, 1998.

[6] D. J. Mulla, "Twenty five years of remote sensing in precision agriculture: Key advances and remaining knowledge gaps," *Biosystems engineering*, vol. 114, no. 4, pp. 358–371, 2013.

[7] M. Govender, K. Chetty, and H. Bulcock, "A review of hyperspectral

remote sensing and its application in vegetation and water resource studies," *Water Sa*, vol. 33, no. 2, 2007.

[8] B. Hörig, F. Kühn, F. Oschütz, and F. Lehmann, "Hymap hyperspectral remote sensing to detect hydrocarbons," *International Journal of Remote Sensing*, vol. 22, no. 8, pp. 1413–1422, 2001.

[9] P. M. Treitz and P. J. Howarth, "Hyperspectral remote sensing for estimating biophysical parameters of forest ecosystems," *Progress in Physical Geography*, vol. 23, no. 3, pp. 359–390, 1999.

[10] S. Veraverbeke, P. Dennison, I. Gitas, G. Hulley, O. Kalashnikova, T. Katagis, L. Kuai, R. Meng, D. Roberts, and N. Stavros, "Hyperspectral remote sensing of fire: State-of-the-art and future perspectives," *Remote Sensing of Environment*, vol. 216, pp. 105–121, 2018.

[11] M. Herold, D. A. Roberts, M. E. Gardner, and P. E. Dennison, "Spectrometry for urban area remote sensingdevelopment and analysis of a spectral library from 350 to 2400 nm," *Remote Sensing of Environment*, vol. 91, no. 3-4, pp. 304–319, 2004.

[12] P. W. Yuen and M. Richardson, "An introduction to hyperspectral imaging and its application for security, surveillance and target acquisition," *The Imaging Science Journal*, vol. 58, no. 5, pp. 241–253, 2010.

[13] J. M. Haut, M. Paoletti, J. Plaza, and A. Plaza, "Cloud implementation of the k-means algorithm for hyperspectral image analysis," *The Journal of Supercomputing*, vol. 73, no. 1, pp. 514–529, 2017.

[14] F. Melgani and L. Bruzzone, "Classification of hyperspectral remote sensing images with support vector machines," *IEEE Transactions on geoscience and remote sensing*, vol. 42, no. 8, pp. 1778–1790, 2004.

[15] J. Li, J. M. Bioucas-Dias, and A. Plaza, "Semisupervised hyperspectral image classification using soft sparse multinomial logistic regression," *IEEE Geoscience and Remote Sensing Letters*, vol. 10, no. 2, pp. 318–322, 2013.

[16] P. Ghamisi, N. Yokoya, J. Li, W. Liao, S. Liu, J. Plaza, B. Rasti, and A. Plaza, "Advances in hyperspectral image and signal processing: A comprehensive overview of the state of the art," *IEEE Geoscience and Remote Sensing Magazine*, vol. 5, no. 4, pp. 37–78, 2017.

[17] P. Ghamisi, J. Plaza, Y. Chen, J. Li, and A. J. Plaza, "Advanced spectral classifiers for hyperspectral images: A review," *IEEE Geoscience and Remote Sensing Magazine*, vol. 5, no. 1, pp. 8–32, 2017.

[18] P. K. Goel, S. O. Prasher, R. M. Patel, J.-A. Landry, R. Bonnell, and A. A. Viau, "Classification of hyperspectral data by decision trees and artificial neural networks to identify weed stress and nitrogen status of corn," *Computers and Electronics in Agriculture*, vol. 39, no. 2, pp. 67–93, 2003.

[19] F. Ratle, G. Camps-Valls, and J. Weston, "Semisupervised neural networks for efficient hyperspectral image classification," *IEEE Transactions on Geoscience and Remote Sensing*, vol. 48, no. 5, pp. 2271–2282, 2010.

[20] G. Cybenko, "Approximation by superpositions of a sigmoidal function," *Mathematics of control, signals and systems*, vol. 2, no. 4, pp. 303–314, 1989.

[21] K. Hornik, "Approximation capabilities of multilayer feedforward networks," *Neural networks*, vol. 4, no. 2, pp. 251–257, 1991.

[22] Y. LeCun, Y. Bengio, and G. Hinton, "Deep learning," *nature*, vol. 521, no. 7553, p. 436, 2015.

[23] L. He, J. Li, C. Liu, and S. Li, "Recent advances on spectralspatial hyperspectral image classification: An overview and new guidelines," *IEEE Transactions on Geoscience and Remote Sensing*, vol. 56, no. 3, pp. 1579–1597, March 2018.

[24] G. Hughes, "On the mean accuracy of statistical pattern recognizers," *IEEE transactions on information theory*, vol. 14, no. 1, pp. 55–63, 1968.

[25] S. Kaewpijit, J. Le Moigne, and T. El-Ghazawi, "Automatic reduction of hyperspectral imagery using wavelet spectral analysis," *IEEE transactions on Geoscience and Remote Sensing*, vol. 41, no. 4, pp. 863–871, 2003.

[26] J. M. Haut, M. E. Paoletti, J. Plaza, and A. Plaza, "Fast dimensionality reduction and classification of hyperspectral images with extreme learning machines," *Journal of Real-Time Image Processing*, pp. 1–24, 2018.

[27] D. J. Field, "Wavelets, vision and the statistics of natural scenes," *Philosophical Transactions of the Royal Society of London A: Mathematical, Physical and Engineering Sciences*, vol. 357, no. 1760, pp. 2527–2542, 1999.

[28] M. E. Paoletti, J. M. Haut, R. Fernandez-Beltran, J. Plaza, A. Plaza, J. Li, and F. Pla, "Capsule networks for hyperspectral image classification," *IEEE Transactions on Geoscience and Remote Sensing*, 2018.

[29] W. Hu, Y. Huang, L. Wei, F. Zhang, and H. Li, "Deep convolutional neural networks for hyperspectral image classification," *Journal of Sensors*, vol. 2015, p. 12, 2015.

[30] J. Yue, W. Zhao, S. Mao, and H. Liu, "Spectral–spatial classification of hyperspectral images using deep convolutional neural networks," *Remote Sensing Letters*, vol. 6, no. 6, pp. 468–477, 2015.

[31] W. Zhao and S. Du, "Spectral–spatial feature extraction for hyperspectral image classification: A dimension reduction and deep learning approach," *IEEE Transactions on Geoscience and Remote Sensing*, vol. 54, no. 8, pp. 4544–4554, 2016.

[32] Y. Chen, H. Jiang, C. Li, X. Jia, and P. Ghamisi, "Deep feature extraction and classification of hyperspectral images based on convolutional neural networks," *IEEE Transactions on Geoscience and Remote Sensing*, vol. 54, no. 10, pp. 6232–6251, 2016.

[33] S. Yu, S. Jia, and C. Xu, "Convolutional neural networks for hyperspectral image classification," *Neurocomputing*, vol. 219, pp. 88–98, 2017.

[34] M. Lin, Q. Chen, and S. Yan, "Network in network," *arXiv preprint arXiv:1312.4400*, 2013.

[35] N. He, M. E. Paoletti, L. Fang, S. Li, A. Plaza, J. Plaza *et al.*, "Feature extraction with multiscale covariance maps for hyperspectral image classification," *IEEE Transactions on Geoscience and Remote Sensing*, no. 99, pp. 1–15, 2018.

[36] M. Paoletti, J. Haut, J. Plaza, and A. Plaza, "A new deep convolutional neural network for fast hyperspectral image classification," *ISPRS Journal of Photogrammetry and Remote Sensing*, vol. 145, pp. 120 – 147, 2018.

[37] J. M. Haut, M. E. Paoletti, J. Plaza, J. Li, and A. Plaza, "Active learning with convolutional neural networks for hyperspectral image classification using a new bayesian approach," *IEEE Transactions on Geoscience and Remote Sensing*, no. 99, pp. 1–22, 2018.

[38] K. He, X. Zhang, S. Ren, and J. Sun, "Deep residual learning for image recognition," in *Proceedings of the IEEE conference on computer vision and pattern recognition*, 2016, pp. 770–778.

[39] X. Glorot and Y. Bengio, "Understanding the difficulty of training deep feedforward neural networks," in *Proceedings of the thirteenth international conference on artificial intelligence and statistics*, 2010, pp. 249–256.

[40] R. K. Srivastava, K. Greff, and J. Schmidhuber, "Training very deep networks," in *Advances in neural information processing systems*, 2015, pp. 2377–2385.

[41] ——, "Highway networks," *arXiv preprint arXiv:1505.00387*, 2015.

[42] G. Huang, Z. Liu, L. Van Der Maaten, and K. Q. Weinberger, "Densely connected convolutional networks," in *Proceedings of the IEEE conference on computer vision and pattern recognition*, 2017, pp. 4700–4708.

[43] K. Zhang, M. Sun, T. X. Han, X. Yuan, L. Guo, and T. Liu, "Residual networks of residual networks: Multilevel residual networks," *IEEE Transactions on Circuits and Systems for Video Technology*, vol. 28, no. 6, pp. 1303–1314, 2018.

[44] J. M. Haut, R. Fernandez-Beltran, M. E. Paoletti, J. Plaza, A. Plaza, and F. Pla, "A new deep generative network for unsupervised remote sensing single-image super-resolution," *IEEE Transactions on Geoscience and Remote Sensing*, no. 99, pp. 1–19, 2018.

[45] K. He, X. Zhang, S. Ren, and J. Sun, "Identity mappings in deep residual networks," in *European conference on computer vision*. Springer, 2016, pp. 630–645.

[46] Z. Zhong, J. Li, Z. Luo, and M. Chapman, "Spectral–spatial residual network for hyperspectral image classification: A 3-d deep learning framework," *IEEE Transactions on Geoscience and Remote Sensing*, vol. 56, no. 2, pp. 847–858, 2018.

[47] M. E. Paoletti, J. M. Haut, R. Fernandez-Beltran, J. Plaza, A. J. Plaza, and F. Pla, "Deep pyramidal residual networks for spectral-spatial hyperspectral image classification," *IEEE Transactions on Geoscience and Remote Sensing*, no. 99, pp. 1–15, 2018.

[48] M. Paoletti, J. Haut, J. Plaza, and A. Plaza, "Deep&dense convolutional neural network for hyperspectral image classification," *Remote Sensing*, vol. 10, no. 9, p. 1454, 2018.

[49] M. Thorpe and Y. van Gennip, "Deep limits of residual neural networks," *arXiv preprint arXiv:1810.11741*, 2018.

[50] L. Ruthotto and E. Haber, "Deep neural networks motivated by partial differential equations," *arXiv preprint arXiv:1804.04272*, 2018.

[51] E. Weinan, "A proposal on machine learning via dynamical systems," *Communications in Mathematics and Statistics*, vol. 5, no. 1, pp. 1–11, 2017.

[52] E. Haber, L. Ruthotto, E. Holtham, and S.-H. Jun, "Learning across scales - multiscale methods for convolution neural networks," in *Thirty-Second AAAI Conference on Artificial Intelligence*, 2018.

[53] Y. Lu, A. Zhong, Q. Li, and B. Dong, "Beyond finite layer neural networks: Bridging deep architectures and numerical differential equations," *arXiv preprint arXiv:1710.10121*, 2017.

[54] T. Q. Chen, Y. Rubanova, J. Bettencourt, and D. K. Duvenaud, "Neural ordinary differential equations," in *Advances in Neural Information Processing Systems 31*. Curran Associates, Inc., 2018, pp. 6572–6583.
[55] M. E. Paoletti, J. M. Haut, J. Plaza, and A. Plaza, "An investigation on self-normalized deep neural networks for hyperspectral image classification," in *IGARSS 2018 - 2018 IEEE International Geoscience and Remote Sensing Symposium*, July 2018, pp. 3607–3610.
[56] I. Goodfellow, Y. Bengio, A. Courville, and Y. Bengio, *Deep learning*. MIT press Cambridge, 2016, vol. 1.
[57] V. Nair and G. E. Hinton, "Rectified linear units improve restricted boltzmann machines," in *Proceedings of the 27th international conference on machine learning (ICML-10)*, 2010, pp. 807–814.
[58] L. Bottou, F. E. Curtis, and J. Nocedal, "Optimization methods for large-scale machine learning," *Siam Review*, vol. 60, no. 2, pp. 223–311, 2018.
[59] J. D. Lambert, *Numerical methods for ordinary differential systems: the initial value problem*. John Wiley & Sons, Inc., 1991.
[60] J. Dormand and P. Prince, "A family of embedded runge-kutta formulae," *Journal of Computational and Applied Mathematics*, vol. 6, no. 1, pp. 19 – 26, 1980.
[61] K. E. Atkinson, *An introduction to numerical analysis*. John wiley & sons, 2008.
[62] J. T. Betts, "Survey of numerical methods for trajectory optimization," *Journal of guidance, control, and dynamics*, vol. 21, no. 2, pp. 193–207, 1998.
[63] R. O. Green, M. L. Eastwood, C. M. Sarture, T. G. Chrien, M. Aronsson, B. J. Chippendale, J. A. Faust, B. E. Pavri, C. J. Chovit, M. Solis, M. R. Olah, and O. Williams, "Imaging spectroscopy and the Airborne Visible/Infrared Imaging Spectrometer (AVIRIS)," *Remote Sensing of Environment*, vol. 65, no. 3, pp. 227–248, 1998.
[64] B. Kunkel, F. Blechinger, R. Lutz, R. Doerffer, H. van der Piepen, and M. Schroder, "ROSIS (Reflective Optics System Imaging Spectrometer) - A candidate instrument for polar platform missions," in *Proc. SPIE 0868 Optoelectronic technologies for remote sensing from space*, J. Seeley and S. Bowyer, Eds., 1988, p. 8.

Mercedes Paoletti (S17) received the B.Sc and M.Sc. degrees in computer engineering from the University of Extremadura, Cáceres, Spain, in 2014 and 2016, respectively. She is currently a Member of the Hyperspectral Computing Laboratory, Department of Technology of Computers and Communications, University of Extremadura, as Ph.D. student, with an University Teacher Training Programme from the Spanish Ministry of Education. Her research interests include remote sensing and analysis of very high spectral resolution with the current focus on deep learning and high performance computing.

She has been reviewer for the IEEE Transactions on Geoscience and Remote Sensing, and IEEE Geoscience and Remote Sensing Letters, and she was a recipient of the 2019 Outstanding Paper Award recognition in WHISPERS 2019 congress.

Juan Mario Haut (S17-M'19) is a member of the Hyperspectral Computing Laboratory at the Department of Technology of Computers and Communications, University of Extremadura, where he received the B.Sc and M.Sc. degrees in computer engineering in 2011 and 2014, respectively, and the Ph.D. degree in Information Technology in 2019 with an University Teacher Training Programme from the Spanish Ministry of Education. His research interests include remote sensing and analysis of very high spectral resolution with the current focus on machine (deep) learning and cloud computing. Dr. Haut has been reviewer for the IEEE Transactions on Geoscience and Remote Sensing, IEEE Journal of Selected Topics in Applied Earth Observations and Remote Sensing, and IEEE Geoscience and Remote Sensing Letters, and he was a recipient of the Best Reviewers recognition of the IEEE Geoscience and Remote Sensing Letters in 2019 and the Outstanding Paper Award in WHISPERS 2019 congress.

Javier Plaza (M09-SM15) is a member of the Hyperspectral Computing Laboratory at the Department of Technology of Computers and Communications, University of Extremadura, where he received the M.Sc. degree in 2004 and the PhD degree in 2008, both in Computer Engineering. He was the recipient of the Outstanding Ph.D. Dissertation Award at the University of Extremadura in 2008. His main research interests comprise hyperspectral data processing and parallel computing of remote sensing data. He has authored more than 150 publications, including over 50 JCR journal papers, 10 book chapters, and 90 peer-reviewed conference proceeding papers. He has guest edited 4 special issues on hyperspectral remote sensing for different journals. He is an Associate Editor for IEEE Geoscience and Remote Sensing Letters and an Associate Editor of the IEEE Remote Sensing Code Library. He is a recipient of the Best Column Award of the IEEE Signal Processing Magazine in 2015 and the most highly cited paper (2005-2010) in the Journal of Parallel and Distributed Computing. He received best paper awards at the IEEE International Conference on Space Technology and the IEEE Symposium on Signal Processing and Information Technology. http://www.umbc.edu/rssipl/people/jplaza

Antonio Plaza (M05-SM07-F15) is the Head of the Hyperspectral Computing Laboratory at the Department of Technology of Computers and Communications, University of Extremadura, where he received the M.Sc. degree in 1999 and the PhD degree in 2002, both in Computer Engineering. His main research interests comprise hyperspectral data processing and parallel computing of remote sensing data. He has authored more than 600 publications, including over 200 JCR journal papers (over 160 in IEEE journals), 23 book chapters, and around 300 peer-reviewed conference proceeding papers. He has guest edited 10 special issues on hyperspectral remote sensing for different journals. Prof. Plaza is a Fellow of IEEE for contributions to hyperspectral data processing and parallel computing of Earth observation data. He is a recipient of the recognition of Best Reviewers of the IEEE Geoscience and Remote Sensing Letters (in 2009) and a recipient of the recognition of Best Reviewers of the IEEE Transactions on Geoscience and Remote Sensing (in 2010), for which he served as Associate Editor in 2007-2012. He is also an Associate Editor for IEEE Access (receiving a recognition as outstanding Associate Editor of the journal in 2017), and was a member of the Editorial Board of the IEEE Geoscience and Remote Sensing Newsletter (2011-2012) and the IEEE Geoscience and Remote Sensing Magazine (2013). He was also a member of the steering committee of the IEEE Journal of Selected Topics in Applied Earth Observations and Remote Sensing (JSTARS). He is a recipient of the Best Column Award of the IEEE Signal Processing Magazine in 2015, the 2013 Best Paper Award of the JSTARS journal, and the most highly cited paper (2005-2010) in the Journal of Parallel and Distributed Computing. He received best paper awards at the IEEE International Conference on Space Technology and the IEEE Symposium on Signal Processing and Information Technology. He served as the Director of Education Activities for the IEEE Geoscience and Remote Sensing Society (GRSS) in 2011-2012, and as President of the Spanish Chapter of IEEE GRSS in 2012-2016. He has reviewed more than 500 manuscripts for over 50 different journals. He served as Editor-in-Chief of the IEEE Transactions on Geoscience and Remote Sensing from 2013 to 2017. Additional information: http://www.umbc.edu/rssipl/people/aplaza